Department of Geomatics Engineering

Accuracy Improvement of Low Cost INS/GPS for Land Applications

(URL: http://www.geomatics.ucalgary.ca/links/GradTheses.html)

by

Eun-Hwan Shin

December, 2001

UNIVERSITY OF
CALGARY

THE UNIVERSITY OF CALGARY

Accuracy Improvement of Low Cost INS/GPS for Land Applications

by

Eun-Hwan Shin

A THESIS

SUBMITTED TO THE FACULTY OF GRADUATE STUDIES

IN PARTIAL FULFILLMENT OF THE REQUIREMENTS

FOR THE DEGREE OF MASTER OF SCIENCE

DEPARTMENT OF GEOMATICS ENGINEERING

CALGARY, ALBERTA

DECEMBER, 2001

Abstract

Since the usage of high performance inertial navigation systems (INSs) is limited by their high price and the regulation by the government, low cost INSs are used for general application areas. However, low cost INSs can experience large positioning errors in very short time due to the low quality of the inertial measuring unit (IMU). To overcome the limitations of low cost INSs, several techniques were developed and tested using the NovAtel Black Diamond System (BDS$^{\text{TM}}$).

A new field calibration method was developed and tested successfully. It is not needed to align the IMU to the local level frame with the method. Furthermore, the bias estimation of the calibration method is not affected by the reference gravity error. Almost half of the positioning error could be removed with the accelerometer calibration information.

The mechanization and navigation Kalman filter were implemented based on the navigation frame to test the velocity matching alignment and non-holonomic constraints. The velocity matching alignment technique was tested for the IMUs to which stationary alignment technique cannot be applied. All attitude components converged within three minutes with RMS 0.03°. Non-holonomic constraints dramatically reduced the horizontal positioning error, within 40 m for 20 minutes operation. Therefore, low cost INSs can be used as a stand-alone positioning system during the GPS outages of over 10 minutes.

Acknowledgements

First of all, I would like to express my sincere gratitude to my supervisor, Dr. Naser El-Sheimy. He continuously encouraged me to go through all the researches during my graduate studies. Special thanks go to Dr. Bruno Scherzinger for reviewing the new calibration method developed in this thesis and providing invaluable suggestions. I would like to acknowledge all the examining committee members for taking time to read my thesis draft. I would like to thank Waypoint Consulting Inc. for providing the GrafNav Software that was used extensively in this thesis.

Kai-Wei Chiang is thanked for his willingness to participate in all the field tests. Bruce Wright, Sameh Nassar, Changlin Ma are also thanked for helping me in preparing the field tests. I would like to acknowledge Mike Bobye for his willingness to provide detailed information about the data format of BDS^{TM} system. I would like to acknowledge Dr. Alexander Bruton for many discussions and advices. Sandra Kennedy and Darren Cosandier are also thanked for the discussion about GPS velocity errors. Michael Kern is thanked for helping me get used to LaTeX.

Finally thanks go to my lovely wife, Su Nam Lee, for her dedication and endurance.

Contents

List of Tables

List of Figures

xiii

List of Symbols, Abbreviations, Nomenclature

The notations used in this thesis follow those widely used in Geomatics and navigation fields.

1. Conventions

   (a) Matrices are denoted as upper case italic letters.

   (b) Vectors are denoted as underlined lower case italic letters.

   (c) The coordinate frames that are involved in the vector transformation are denoted as subscript and superscript. For instance, C_b^n is the direction cosine matrix from the body frame to the navigation frame. For the angular rate vector subscript denotes the reference and target frame, and superscript denotes the projected or realized frame. For example, $\underline{\omega}_{ib}^n$ represents the angular rate vector of the body frame with respect to the inertial frame projected to the navigation frame.

(d) Operators are defined as:

$\cdot$ time derivative

$\hat{\ }$ estimated or computed values

$\tilde{\ }$ measured values

$\bar{\ }$ Kalman prediction

δ error of, correction to

$\delta(\ )$ Dirac delta function

Δ increment of

$^{-1}$ matrix inverse

^{T} matrix transpose

$<\ \ >$ inner product

$\times$ cross product

$(\ \times)$ cross product or skew symmetric form of a vector

$diag()$ diagonal matrix

$E[\ ]$ expectation

$f(\ )$ is a function of

$\mathcal{L}^{-1}()$ inverse Laplace transform

2. Symbols

$0_{3\times3}$ 3×3 zero matrix

$\underline{\epsilon}$	attitude error vector
γ	normal gravity
λ	geodetic longitude
$\underline{\omega}$	angular rate vector
Ω	cross product or skew symmetric matrix form of $\underline{\omega}$
φ	geodetic latitude
ϕ	roll
Φ	transition matrix
θ	pitch, non-orthogonality of IMU axes
ψ	heading
a	semi-major axis of the reference ellipsoid
A	design matrix
b	bias
B	design matrix
C	direction cosine matrix, covariance matrix
e	linear eccentricity of the reference ellipsoid
$\underline{e}$	measurement noise vector
E	cross product or skew symmetric matrix form of $\underline{\epsilon}$
$\underline{f}$	specific force vector
F	dynamics matrix

$\bar{g}$	gravitational acceleration vector
$\underline{g}$	gravity vector
G	design matrix of system noise vector
h	ellipsoidal height
H	design matrix for measurements
I	identity matrix
$I_{3\times3}$	3×3 identity matrix
K	Kalman gain matrix
ℓ	measurements
m	order of interpolation or extrapolation
M	radius of curvature in meridian
N	radius of curvature in prime vertical,
	coefficient matrix of the normal equation
P	covariance matrix of state vector
$\underline{q}$	quaternion vector
Q_k	covariance matrix of system noise sequence vector
$Q(t)$	spectral density matrix
$\underline{r}$	position vector, residual vector
R	rotation matrix of coordinate systems or vectors,
	covariance matrix of measurement error vector

s	scale factor
$\underline{u}$	continuous time system noise vector
$\underline{v}$	velocity vector
$\Delta\underline{v}_f$	velocity increment vector which is not corrected for the Coriolis and gravity force
$\underline{w}$	system noise sequence vector, misclosure vector
$\underline{x}$	state vector, x-axis
$\underline{y}$	y-axis
$\underline{z}$	measurement vector, z-axis

3. Acronyms

BDS^{TM}	Black Diamond System
DCM	Direction Cosine Matrix
ENU	East-North-Up
FOG	Fibre Optic Gyroscope
GPS	Global Positioning System
IMU	Inertial Measuring Unit
INS	Inertial Navigation System
MEMS	Micro Electrical Mechanical Systems
NED	North-East-Down

Chapter 1

Introduction

1.1 Background and Objective

The integration of a navigation-grade inertial navigation system (INS) with the global positioning system (GPS) has been done for the application areas in which attitude information is indispensable and rapid collection of geographic information is required. In practice, integration is necessary for navigation in urban areas where the signal from the satellites is susceptible to blocking by many obstacles (such as skyscrapers, trees, etc.). However, there are two restrictions in using high performance INSs. One is their price, over US$100,000, and the other is a regulation by the government. Hence, a high performance INS is usually used in military applications and commercial airliners, and is not suitable for general pur-

pose application areas such as car navigation or general aviation (Gebre-Egziabher *et al.*, 2001). Therefore, recent research efforts have been focused on using low cost inertial measuring units (IMUs), for instance see Zhang (1995), Škaloud *et al.* (1997), Wolf *et al.* (1997), Salychev *et al.* (2000), and Sukkarieh (2000).

Zhang (1995), Wolf *et al.* (1997), and Salychev *et al.* (2000) discussed the integration of a Systron Donner's Motionpak$^{\text{TM}}$ IMU with one or more GPS antennas. Salychev *et al.* (2000) used external heading information to align the IMU. Sukkarieh (2000) proposed the use of non-holonomic constraints, which describe the characteristics of the motion of land vehicles. Motion of a wheeled vehicle on a surface is governed by two non-holonomic constraints (Sukkarieh, 2000, p. 94), i.e. vehicles do not move upward/downward direction, and lateral velocity is almost zero.

Low cost IMUs are peculiar in their weak stand-alone accuracy and poor run-to-run stability (Salychev *et al.*, 2000), which can result in large errors over short time intervals if their errors are not compensated. The IMU itself costs, roughly speaking, under US\$10,000 and the price is decreasing continuously with the development of Micro Electrical Mechanical Systems (MEMS) technology. Table 1.1 compares the performance of IMUs from the navigation-grade to consumer-grade.

For example, the biases of the accelerometers of a Crossbow DMU-FOG IMU is usually up to 1,000 $mGal$ (0.01 m/s^2) and they drift with the change of temperature. Also, the level

Table 1.1: INS performance (Schwarz and El-Sheimy, 1999; Greenspan, 1995; Gebre-Egziabher *et al.*, 2001)

Grade		Navigation	Tactical	Automotive	Consumer
Position error		1.9 (km/hr)	19-38 (km/hr)	≈2 (km/min)	≈3 (km/min)
Gyro	bias (deg/hr)	0.005-0.01	1-10	180	360
	scale factor (ppm)	5-50	200-500		
	noise (deg/hr/$\sqrt{\text{Hz}}$)	0.002-0.005	0.2-0.5		
Accel	bias (μg)	5-10	200-500	1200	2400
	scale factor (ppm)	10-20	400-1000		
	noise (μg/hr/$\sqrt{\text{Hz}}$)	5-10	200-400		

of the bias and noise of the gyroscopes is very high. For instance, as analyzed in Section 4.2.1, the gyroscope bias level of a Honeywell HG1700 IMU is rated at 1 $°/hr$, which can cause a 6° initial heading error in mid-latitude areas. The gyroscope bias and noise level of the Crossbow DMU-FOG IMUs are higher than the magnitude of the Earth's rotation rate signal, and therefore, the attitude initialization with gyro-compassing is impossible.

Hence, the estimation of gyroscope biases plays a significant role for tactical-grade IMUs, and the augmentation with other sensors, for instance multi-GPS antennas and magnetic sensors, is needed to initialize the attitude of automotive-grade or consumer-grade IMUs.

A new calibration technique was developed by Shin and El-Sheimy (2002), which does not require the IMU to be aligned with respect to the local-level frame and therefore it is easy to use in the field. In case there is only one GPS antenna, the attitude of an IMU can be initialized by the GPS velocity aiding, see for instance Titterton and Weston (1997, p. 276) and Farrell and Barth (1998, p. 233). Since heading is susceptible to drift when the vehicle's velocity is zero due to the low quality of the gyroscopes, a technique to limit the attitude error growth is needed for the time when the host vehicle is not moving, such as waiting for a traffic signal.

The objective of the thesis is to improve the accuracy of low cost INS systems so that they can be used as a stand-alone navigation system during long GPS outages for general ground vehicle navigation. To accomplish this objective, the following techniques will be developed and tested:

- **field calibration methods**: estimates the biases and scale factors of the IMU in the field

- **velocity matching alignment**: initializes the attitude of an IMU using GPS velocity information

- **using the non-holonomic constraints**: reduces stand-alone positioning accuracy

For testing the velocity matching alignment and non-holonomic constraints, an INS mecha-

nization and a navigation Kalman filter have been developed.

1.2 Thesis Outline

Chapter 2 derives the navigation frame inertial navigation equations. The navigation frame is chosen because the elements of the state vector, derived in Chapter 3, carry physical meanings which are easy to visualize. After defining various reference frames, the inertial navigation equations will be derived. The discrete time mechanization equations are given in the final section. The error equations shall be derived based on these navigation equations.

Chapter 3 derives the error dynamics equations, for use in the Kalman filter, based on the perturbation analysis for position, velocity and attitude errors. Then, various issues, which have to be considered in the implementation of the INS/GPS integration Kalman filter, will be discussed such as the lever-arm correction, resolving the time difference between the IMU and GPS measurements, and the feedback of the estimated states.

Chapter 4 discusses various techniques to improve the accuracy of low cost INS/GPS systems. A new calibration method will be introduced to estimate the biases and scale factors in the field. The sensitivity of the method in using erroneous reference gravity values is discussed as well. The velocity matching alignment method will be described using a five-state Kalman filter. The equations to use the non-holonomic constraints in the navigation Kalman filter

will be derived based on the perturbation analysis. Finally, the methods to limit attitude error growth will be discussed.

Chapter 5 holds the test results using the NovAtel Black Diamond System (BDS^{TM}), which integrates a NovAtel OEM4 GPS receiver and a Honeywell HG1700 IMU (NovAtel, Inc., 2001). The new calibration method is applied in the field and the effect of the calibration on the positioning accuracy is also discussed. The performance of the newly developed navigation frame INS mechanization is compared to that of the KINGSPAD^{TM} software. The errors of the velocity matching alignment method and the non-holonomic constraints were analyzed.

Finally, Chapter 6 will conclude the thesis as well as will give some recommendations for future work.

Chapter 2

Terrestrial Inertial Navigation Mechanization

Over 20 years of worldwide developments in strapdown inertial navigation algorithms were summarized by Savage (1998a,b) and recently new approaches to accommodate modern computer technologies were started by Litmanovich *et al.* (2000). However, these efforts are mainly for high performance inertial navigation systems (strategic-grade or navigation-grade). This chapter will provide the INS mechanization equations which can be applied to both navigation-grade or lower grade IMUs. In the first section, various coordinate frames will be defined and the transformation between them will be given. The navigation equations are developed on the basis of the navigation frame, which are widely used in the navigation

society. Finally, the discrete time INS mechanization will be given.

2.1   Reference Frames and Transformations

The inertial frame (*i*-frame) has its origin at the centre of the Earth and axes which are non-rotating with respect to the fixed stars with its z-axis parallel to the spin axis of the Earth, x-axis pointing towards the mean vernal equinox, and y-axis completing a right-handed orthogonal frame as shown in Figure 2.1. The vernal equinox is the ascending node between the celestial equator and the ecliptic. So, the right ascension system is used as the inertial frame in practice, since it closely approximates an inertial frame (Schwarz, 1999, p. 114).
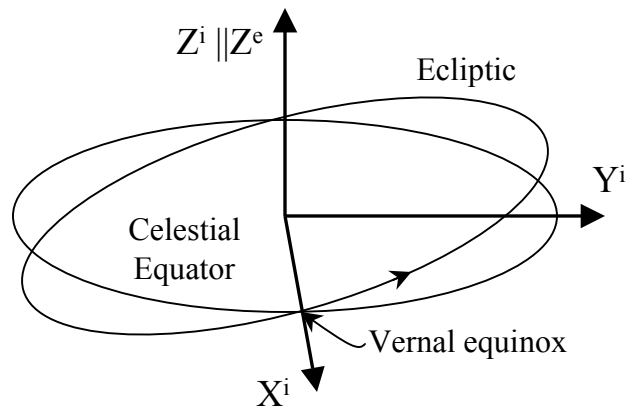
Figure 2.1: The inertial frame

The Earth frame (*e*-frame) has its origin at the centre of mass of the Earth and axes which are fixed with respect to the Earth. Its x-axis points towards the mean meridian of Greenwich, z-axis is parallel to the mean spin axis of the Earth, and y-axis completes a right-handed orthogonal frame.

The navigation frame (*n*-frame) is a local geodetic frame which has its origin coinciding with that of the sensor frame, and axes with x-axis pointing towards geodetic north, z-axis orthogonal to the reference ellipsoid pointing down, and y-axis completing a right-handed orthogonal frame, i.e. the north-east-down (NED) system as shown in Figure 2.2. The benefit of the east-north-up (ENU) system is that altitude increases in the upward. The advantages of NED system are that the direction of a right turn is in the positive direction with respect to a downward axis, and the axes coincide with vehicle-fixed roll-pitch-heading coordinates when the vehicle is level and headed north (Grewal *et al.*, 2001, p. 338). Further, NED system is prevalent and therefore more research results can be found and incorporated into one's own directly.

The body frame (*b*-frame) is an orthogonal axis set which is aligned with the roll, pitch and heading axes of a vehicle, i.e. forward-transversal-down as shown in Figure 2.3.
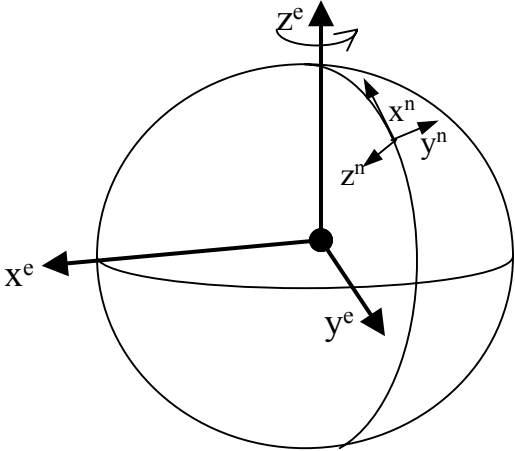
Figure 2.2: The Earth frame and the navigation frame
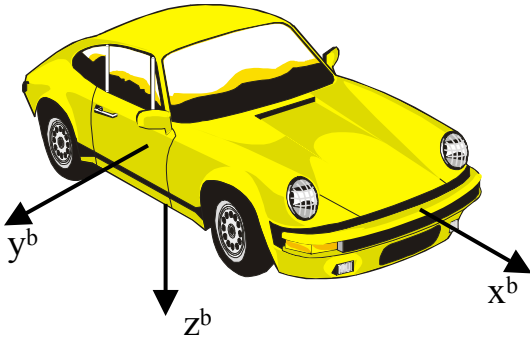
Figure 2.3: The body frame

The direction cosine matrix (DCM) from the e-frame to the n-frame can be expressed as:

$$
\begin{aligned}
C_e^n &= R_y(-\varphi - \pi/2)R_z(\lambda) \\[2mm]
&= \begin{pmatrix} -\sin\varphi\cos\lambda & -\sin\varphi\sin\lambda & \cos\varphi \\[2mm] -\sin\lambda & \cos\lambda & 0 \\[2mm] -\cos\varphi\cos\lambda & -\cos\varphi\sin\lambda & -\sin\varphi \end{pmatrix}
\end{aligned}
\tag{2.1}
$$

where, φ is latitude, λ is longitude, R_y and R_z denote rotation of coordinate systems about y-axis and z-axis, respectively. Then, the DCM from the n-frame to the e-frame can be obtained using the orthogonality as:

$$
C_n^e = (C_e^n)^T = \begin{pmatrix} -\sin\varphi\cos\lambda & -\sin\lambda & -\cos\varphi\cos\lambda \\[2mm] -\sin\varphi\sin\lambda & \cos\lambda & -\cos\varphi\sin\lambda \\[2mm] \cos\varphi & 0 & -\sin\varphi \end{pmatrix}
\tag{2.2}
$$

The definition for the DCM from the n-frame to the b-frame is given as (Titterton and Weston, 1997, p.44):

$$
C_n^b = R_x(\phi)R_y(\theta)R_z(\psi)
\tag{2.3}
$$

where, ϕ, θ, and ψ are the three components of the Euler angles roll, pitch, and heading, respectively. Hence, the DCM from the b–frame to the n–frame is obtained again using the

orthogonality:

$$
C_b^n = \left(C_n^b\right)^T = R_z(-\psi)R_y(-\theta)R_x(-\phi)
$$

$$
= \begin{pmatrix} \cos\psi & -\sin\psi & 0 \\ \sin\psi & \cos\psi & 0 \\ 0 & 0 & 1 \end{pmatrix} \begin{pmatrix} \cos\theta & 0 & \sin\theta \\ 0 & 1 & 0 \\ -\sin\theta & 0 & \cos\theta \end{pmatrix} \begin{pmatrix} 1 & 0 & 0 \\ 0 & \cos\phi & -\sin\phi \\ 0 & \sin\phi & \cos\phi \end{pmatrix}
$$

$$
= \begin{pmatrix} c\theta c\psi & -c\phi s\psi + s\phi s\theta c\psi & s\phi s\psi + c\phi s\theta c\psi \\ c\theta s\psi & c\phi c\psi + s\phi s\theta s\psi & -s\phi c\psi + c\phi s\theta s\psi \\ -s\theta & s\phi c\theta & c\phi c\theta \end{pmatrix} \tag{2.4}
$$

where sin and cos are denoted as s and c, respectively.

The Euler angles can also be determined from the DCM C_b^n by the following equations (Farrell and Barth, 1998, p.46):

$$
\theta = -\tan^{-1}\left(\frac{c_{31}}{\sqrt{1 - c_{31}^2}}\right) \tag{2.5}
$$

$$
\phi = atan2(c_{32}, c_{33}) \tag{2.6}
$$

$$
\psi = atan2(c_{21}, c_{11}) \tag{2.7}
$$

where, c_{ij}'s, $1 \leq i, j \leq 3$ are the (i,j)-th elements of the DCM C_b^n and *atan2* is a four quadrant inverse tangent function.

The rotation rate vector of the e-frame with respect to the i-frame projected to the e–frame is given as:

$$\underline{\omega}_{ie}^{e} = \begin{pmatrix} 0 & 0 & \omega_{e} \end{pmatrix}^{T} \tag{2.8}$$

where, ω_{e} is the magnitude of the rotation rate of the Earth and has the value 7.2921158 rad/s. Projecting the vector to the n-frame using Eq. (2.1) makes

$$\underline{\omega}_{ie}^{n} = C_{e}^{n}\underline{\omega}_{ie}^{e} = \begin{pmatrix} \omega_{e}\cos\varphi & 0 & -\omega_{e}\sin\varphi \end{pmatrix}^{T}. \tag{2.9}$$

The transport rate represents the turn rate of the n-frame with respect to the e-frame and is expressed in terms of the rate of change of latitude and longitude as (Titterton and Weston, 1997, p. 52):

$$\underline{\omega}_{en}^{n} = \begin{pmatrix} \dot{\lambda}\cos\varphi & -\dot{\varphi} & -\dot{\lambda}\sin\varphi \end{pmatrix}^{T} \tag{2.10}$$

Writing $\dot{\varphi} = v_{N}/(M+h)$ and $\dot{\lambda} = v_{E}/(N+h)\cos\varphi$,

$$\underline{\omega}_{en}^{n} = \begin{pmatrix} v_{E}/(N+h) \\ -v_{N}/(M+h) \\ -v_{E}\tan\varphi/(N+h) \end{pmatrix} \tag{2.11}$$

where v_{N}, v_{E} are velocities in the north and east direction, respectively. h is ellipsoidal height and M, N are radii of curvature in the meridian and prime vertical given by Schwarz

and Wei (2000, p. 25):

$$N = \frac{a}{(1 - e^2 \sin^2 \varphi)^{1/2}} \tag{2.12}$$

$$M = \frac{a(1 - e^2)}{(1 - e^2 \sin^2 \varphi)^{3/2}} \tag{2.13}$$

where a and e are the semi-major axis and linear eccentricity of the reference ellipsoid, respectively

The equation for $\underline{\omega}_{in}^n$ can be obtained by adding equations (2.9) and (2.11)

$$
\begin{aligned}
\underline{\omega}_{in}^n &= \underline{\omega}_{ie}^n + \underline{\omega}_{en}^n \\
&= \begin{pmatrix} \omega_e \cos \varphi + v_E/(N+h) \\ -v_N/(M+h) \\ -\omega_e \sin \varphi - v_E \tan \varphi/(N+h) \end{pmatrix}
\end{aligned}
\tag{2.14}
$$

shown as functions of the positions and velocities.

2.2 Inertial Navigation Equations

The position in the n-frame is expressed by curvilinear coordinates:

$$\underline{r}^n = (\begin{array}{ccc} \varphi & \lambda & h \end{array})^T \tag{2.15}$$

and the velocities in the n–frame are defined by

$$\underline{v}^n = \begin{pmatrix} v_N \\ v_E \\ v_D \end{pmatrix} = \begin{pmatrix} (M+h) & 0 & 0 \\ 0 & (N+h)\cos\varphi & 0 \\ 0 & 0 & -1 \end{pmatrix} \begin{pmatrix} \dot{\varphi} \\ \dot{\lambda} \\ \dot{h} \end{pmatrix} \tag{2.16}$$

Hence, the time derivative of the coordinates can be written as

$$\underline{\dot{r}}^n = \begin{pmatrix} \dot{\varphi} \\ \dot{\lambda} \\ \dot{h} \end{pmatrix} = \begin{pmatrix} \dfrac{1}{M+h} & 0 & 0 \\ 0 & \dfrac{1}{(N+h)\cos\varphi} & 0 \\ 0 & 0 & -1 \end{pmatrix} \begin{pmatrix} v_N \\ v_E \\ v_D \end{pmatrix} \tag{2.17}$$

To get the velocity dynamics equations, we start with

$$\underline{v}^n = C_e^n \underline{\dot{r}}^e \tag{2.18}$$

Substituting $\underline{\dot{r}}^e = C_i^e(\underline{\dot{r}}^i - \Omega_{ie}^i \underline{r}^i)$ into the above equation yields

$$\underline{v}^n = C_i^n(\underline{\dot{r}}^i - \Omega_{ie}^i \underline{r}^i) \tag{2.19}$$

Hence, the velocity dynamics can be obtained as follows:

$$\begin{aligned} \underline{\dot{v}}^n &= C_i^n \Omega_{ni}^i(\underline{\dot{r}}^i - \Omega_{ie}^i \underline{r}^i) + C_i^n(\underline{\ddot{r}}^i - \Omega_{ie}^i \underline{\dot{r}}^i) \\ &= C_i^n \underline{\ddot{r}}^i + C_i^n(\Omega_{ni}^i - \Omega_{ie}^i)\underline{\dot{r}}^i - C_i^n \Omega_{ni}^i \Omega_{ie}^i \underline{r}^i \end{aligned} \tag{2.20}$$

where the Earth's rotation rate, Ω_{ie}^i, is considered as a constant. Substituting $\underline{\dot{r}}^i = C_e^i(\underline{\dot{r}}^e + \Omega_{ie}^e\underline{r}^e)$ and $I = C_n^i C_i^n$ into the above equation yields

$$
\begin{aligned}
\underline{\dot{v}}^n &= C_i^n\underline{\ddot{r}}^i + C_i^n(\Omega_{ni}^i - \Omega_{ie}^i)C_n^i C_i^n C_e^i(\underline{\dot{r}}^e + \Omega_{ie}^e\underline{r}^e) - C_i^n\Omega_{ni}^i\Omega_{ie}^i\underline{r}^i \\
&= C_i^n\underline{\ddot{r}}^i + (\Omega_{ni}^n - \Omega_{ie}^n)C_e^n\underline{\dot{r}}^e + (\Omega_{ni}^n - \Omega_{ie}^n)C_e^n\Omega_{ie}^e\underline{r}^e - C_i^n\Omega_{ni}^i\Omega_{ie}^i\underline{r}^i \\
&= C_i^n\underline{\ddot{r}}^i + (\Omega_{ni}^n - \Omega_{ie}^n)C_e^n\underline{\dot{r}}^e + \Omega_{ni}^n C_e^n\Omega_{ie}^e\underline{r}^e - \Omega_{ie}^n C_e^n\Omega_{ie}^e\underline{r}^e - C_i^n\Omega_{ni}^i\Omega_{ie}^i\underline{r}^i
\end{aligned}
\tag{2.21}
$$

Using

$$
\begin{aligned}
\Omega_{ni}^n C_e^n\Omega_{ie}^e\underline{r}^e &= C_i^n C_n^i\Omega_{ni}^n C_i^n C_n^i C_e^n\Omega_{ie}^e C_i^e C_e^i\underline{r}^e \\
&= C_i^n\Omega_{ni}^i\Omega_{ie}^i\underline{r}^i
\end{aligned}
$$

and Eq. (2.18) the velocity dynamics can be reduced to

$$
\begin{aligned}
\underline{\dot{v}}^n &= C_i^n\underline{\ddot{r}}^i + (\Omega_{ni}^n - \Omega_{ie}^n)\underline{v}^n - \Omega_{ie}^n C_e^n\Omega_{ie}^e\underline{r}^e \\
&= C_i^n\underline{\ddot{r}}^i - (2\Omega_{ie}^n + \Omega_{en}^n)\underline{v}^n - C_e^n\Omega_{ie}^e\Omega_{ie}^e\underline{r}^e
\end{aligned}
\tag{2.22}
$$

Substituting $\underline{\ddot{r}}^i = \underline{f}^i + \underline{\bar{g}}^i$ into the upper equation yields

$$
\begin{aligned}
\underline{\dot{v}}^n &= C_i^n(\underline{f}^i + \underline{\bar{g}}^i) - (2\Omega_{ie}^n + \Omega_{en}^n)\underline{v}^n - C_e^n\Omega_{ie}^e\Omega_{ie}^e\underline{r}^e \\
&= C_i^n\underline{f}^i - (2\Omega_{ie}^n + \Omega_{en}^n)\underline{v}^n + C_e^n(\underline{\bar{g}}^e - \Omega_{ie}^e\Omega_{ie}^e\underline{r}^e) \\
&= C_b^n\underline{f}^b - (2\Omega_{ie}^n + \Omega_{en}^n)\underline{v}^n + \underline{g}^n
\end{aligned}
\tag{2.23}
$$

where $\underline{f}$ is the specific force vector defined as the difference between the true acceleration in space and the acceleration due to gravity (Titterton and Weston, 1997, p. 10) and $\bar{g}$ is the gravitational acceleration and $\underline{g}$ is the gravity vector. Eq. (2.23) can also be expressed as

$$\underline{\dot{v}}^n = C_b^n \underline{f}^b - (2\underline{\omega}_{ie}^n + \underline{\omega}_{en}^n) \times \underline{v}^n + \underline{g}^n \tag{2.24}$$

Similar derivations can be found in Rogers (2000, p. 73).

The attitude dynamics are defined by Schwarz and Wei (2000, p. 38)

$$\dot{C}_b^n = C_b^n \Omega_{nb}^b = C_b^n (\Omega_{ib}^b - \Omega_{in}^b) \tag{2.25}$$

or by Rogers (2000, p. 74)

$$\dot{C}_b^n = -\Omega_{bn}^n C_b^n \tag{2.26}$$

where Ω represents the skew symmetric matrix form of the vector $\underline{\omega}$ and Ω_{ib}^b is the outputs of the strapdown gyroscopes. Ω_{bn}^n is obtained by

$$\underline{\omega}_{bn}^n = \underline{\omega}_{in}^n - C_b^n \underline{\omega}_{ib}^b \tag{2.27}$$

For the case where the quality of the gyroscope is so crude that we can disregard the Earth's rotation rate, $\underline{\omega}_{in}^n$ may be approximated by $\underline{\omega}_{en}^n$.

Usually quaternion implementation is preferred in updating the attitude as the linearity of the quaternion differential equations, the lack of trigonometric functions, and the small number of parameters allow efficient implementation (Farrell and Barth, 1998, p. 41). The quaternion attitude representation is a four-parameter representation based on the idea that a transformation from one coordinate frame to another may be effected by a single rotation about a vector $\underline{\mu}$ (Titterton and Weston, 1997, p. 46). A quaternion is a four–element vector

$$
\underline{q} = \begin{pmatrix} q_1 \\ q_2 \\ q_3 \\ q_4 \end{pmatrix} = \begin{pmatrix} (\mu_x/\mu)\sin(\mu/2) \\ (\mu_y/\mu)\sin(\mu/2) \\ (\mu_z/\mu)\sin(\mu/2) \\ \cos(\mu/2) \end{pmatrix},
\tag{2.28}
$$

where μ_x, μ_y, μ_z are components of the rotation angle vector $\underline{\mu}$, and $\mu = (\mu_x^2 + \mu_y^2 + \mu_z^2)^{1/2}$. The quaternions should satisfy the following normality condition

$$
q_1^2 + q_2^2 + q_3^2 + q_4^2 = 1.
\tag{2.29}
$$

When this condition is not fulfilled, the normalization of the quaternion can be applied

$$
\hat{\underline{q}} = \underline{q}/\sqrt{\underline{q}^T \underline{q}}.
\tag{2.30}
$$

However, the normalization cannot correct for errors that have occurred in the previous computation cycle. In fact, an error arising in a single element of the quaternion can be

spread amongst all of the elements (Titterton and Weston, 1997, p. 310).

The differential equations for the quaternion parameters is given by (Schwarz and Wei, 2000, p. 46)

$$
\dot{\underline{q}} = \frac{1}{2}
\begin{pmatrix}
0 & \omega_z & -\omega_y & \omega_x \\
-\omega_z & 0 & \omega_x & \omega_y \\
\omega_y & -\omega_x & 0 & \omega_z \\
-\omega_x & -\omega_y & -\omega_z & 0
\end{pmatrix}
\underline{q},
\tag{2.31}
$$

where $\underline{\omega} = (\ \omega_x\ \ \omega_y\ \ \omega_z\ )^T$ is the angular velocity of the body rotation.

The transformations between the quaternion and the DCM C_b^n are accomplished by

$$
C_b^n =
\begin{pmatrix}
(q_1^2 - q_2^2 - q_3^2 + q_4^2) & 2(q_1 q_2 - q_3 q_4) & 2(q_1 q_3 - q_2 q_4) \\
2(q_1 q_2 + q_3 q_4) & (q_2^2 - q_1^2 - q_3^2 + q_4^2) & 2(q_2 q_3 - q_1 q_4) \\
2(q_1 q_3 - q_2 q_4) & 2(q_2 q_3 + q_1 q_4) & (q_3^2 - q_1^2 - q_2^2 + q_4^2)
\end{pmatrix},
\tag{2.32}
$$

and

$$
\underline{q} =
\begin{pmatrix}
q_1 \\
q_2 \\
q_3 \\
q_4
\end{pmatrix}
=
\begin{pmatrix}
0.25(c_{32} - c_{23})/0.5\sqrt{1 + c_{11} + c_{22} + c_{33}} \\
0.25(c_{13} - c_{31})/0.5\sqrt{1 + c_{11} + c_{22} + c_{33}} \\
0.25(c_{21} - c_{12})/0.5\sqrt{1 + c_{11} + c_{22} + c_{33}} \\
0.5\sqrt{1 + c_{11} + c_{22} + c_{33}}
\end{pmatrix}
\tag{2.33}
$$

where c_{ij}'s, $1 \leq i, j \leq 3$ are the (i,j)-th elements of the DCM C_b^n. An efficient algorithm with built-in normalization for the calculation of the DCM from the quaternion can be found in Farrell and Barth (1998, p.41).

In summary, using Eq. (2.17), (2.24) and (2.25), the navigation frame inertial navigation equations can be described as

$$
\begin{pmatrix}
\underline{\dot{r}}^n \\
\underline{\dot{v}}^n \\
\dot{C}_b^n
\end{pmatrix}
=
\begin{pmatrix}
D^{-1}\underline{v}^n \\
C_b^n \underline{f}^b - (2\underline{\omega}_{ie}^n + \underline{\omega}_{en}^n) \times \underline{v}^n + \underline{g}^n \\
C_b^n (\Omega_{ib}^b - \Omega_{in}^b)
\end{pmatrix}
\tag{2.34}
$$

where

$$
D^{-1} =
\begin{pmatrix}
\dfrac{1}{M + h} & 0 & 0 \\
0 & \dfrac{1}{(N + h)\cos\varphi} & 0 \\
0 & 0 & -1
\end{pmatrix}
$$

2.3 INS Mechanization

Strapdown IMUs work in discrete form and they usually output angle and velocity increments in the body frame, i.e. $\Delta\underline{\tilde{\theta}}_{ib}^b$ and $\Delta\underline{\tilde{v}}_f^b$. Therefore, discrete integration algorithms are usually applied to transform these measurements into navigation quantities.

2.3.1 Error Compensation

The gyroscope and accelerometer outputs will be corrected using the bias model and the bias and scale factor model, respectively. Section 4.1 describes the estimation of the biases and scale factors in detail.

$$\Delta\underline{\theta}_{ib}^b = \Delta\tilde{\underline{\theta}}_{ib}^b - \underline{b}_\omega \Delta t \tag{2.35}$$

$$\Delta\underline{v}_f = \begin{pmatrix} 1/(1+s_{gx}) & 0 & 0 \\ 0 & 1/(1+s_{gy}) & 0 \\ 0 & 0 & 1/(1+s_{gz}) \end{pmatrix} (\Delta\tilde{\underline{v}}_f - \underline{b}_g \Delta t) \tag{2.36}$$

where $\Delta\underline{\theta}_{ib}^b$ and $\Delta\underline{v}_f$ are the corrected outputs of the gyroscopes and accelerometers, respectively. $\underline{b}_\omega$ and $\underline{b}_g$ are the vectors of the gyroscope and accelerometer biases, respectively. s_{gx}, s_{gy}, and s_{gz} are the scale factors of the accelerometers. $\Delta t = t_{k+1} - t_k$ is the time increment for the time interval (t_k, t_{k+1}). The sampling rate is usually denoted with the unit $Hz = 1/\Delta t$. As shown in Figure 2.4, the nominal sampling rate of the HG1700 IMU is 100 Hz, but actually it is fluctuating within $\pm 1\%$ range. So, Δt is treated as a variable.
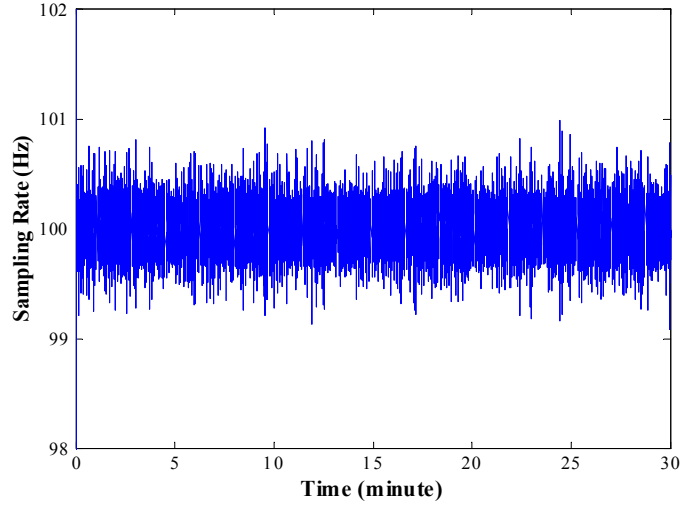
Figure 2.4: Sampling rate of HG1700 IMU

2.3.2   Attitude Integration

The body angular increment with respect to the navigation frame are obtained by

$$
\begin{aligned}
\Delta\underline{\theta}^b_{nb} &= \begin{pmatrix} \Delta\theta_x & \Delta\theta_y & \Delta\theta_z \end{pmatrix}^T \\
&= \Delta\underline{\theta}^b_{ib} - C^b_n(\underline{\omega}^n_{ie} + \underline{\omega}^n_{en})\Delta t
\end{aligned}
\tag{2.37}
$$

and the magnitude of the angular increment is calculated

$$
\Delta\theta = \sqrt{\Delta\theta_x^2 + \Delta\theta_y^2 + \Delta\theta_z^2}
\tag{2.38}
$$

The angular increments obtained in Eq. (2.37) and (2.38) are used to update the quaternion

(Schwarz and Wei, 2000, p. 53):

$$
\underline{q}_{k+1} = \underline{q}_{k} + 0.5 \begin{pmatrix} c & s\Delta\theta_z & -s\Delta\theta_y & s\Delta\theta_x \\ -s\Delta\theta_z & c & s\Delta\theta_x & s\Delta\theta_y \\ s\Delta\theta_y & -s\Delta\theta_x & c & s\Delta\theta_z \\ -s\Delta\theta_x & -s\Delta\theta_y & -s\Delta\theta_z^b & c \end{pmatrix} \underline{q}_k \tag{2.39}
$$

where

$$
s = \frac{2}{\Delta\theta}\sin\frac{\Delta\theta}{2} = 1 - \frac{\Delta\theta^2}{24} + \frac{\Delta\theta^4}{1920} + \cdots
$$

$$
c = 2(\cos\frac{\Delta\theta}{2} - 1) = -\frac{\Delta\theta^2}{4} + \frac{\Delta\theta^4}{192} + \cdots
$$

Finally the DCM C_b^n is updated using Eq. (2.32).

2.3.3   Velocity and Position Integration

The body frame velocity increment due to the specific force is transformed to the navigation frame through (Schwarz and Wei, 2000, p. 55):

$$
\Delta\underline{v}_f^n = C_b^n \begin{pmatrix} 1 & 0.5\Delta\theta_z & -0.5\Delta\theta_y \\ -0.5\Delta\theta_z & 1 & 0.5\Delta\theta_x \\ 0.5\Delta\theta_y & -0.5\Delta\theta_x & 1 \end{pmatrix} \Delta\underline{v}_f^b \tag{2.40}
$$

where the first order sculling correction is applied. Then, the velocity increment is obtained by applying the Coriolis and gravity correction:

$$\Delta \underline{v}^n = \Delta \underline{v}_f^n - (2\underline{\omega}_{ie}^n + \underline{\omega}_{en}^n) \times \underline{v}^n \Delta t + \underline{\gamma}^n \Delta t \tag{2.41}$$

where $\underline{\gamma}^n = \begin{pmatrix} 0 & 0 & \gamma \end{pmatrix}^T$, and γ is the normal gravity at the geodetic latitude φ and ellipsoidal height h (Schwarz and Wei, 2000, p. 30)

$$\gamma = a_1(1 + a_2 \sin^2 \varphi + a_3 \sin^4 \varphi) + (a_4 + a_5 \sin^2 \varphi)h + a_6 h^2 \tag{2.42}$$

$$a_1 = 9.7803267715 \qquad a_4 = \text{-0.0000030876910891}$$

$$a_2 = 0.0052790414 \qquad a_5 = 0.0000000043977311$$

$$a_3 = 0.0000232718 \qquad a_6 = 0.0000000000007211$$

The velocity integration can be performed as

$$\underline{v}_{k+1}^n = \underline{v}_k^n + \Delta \underline{v}_{k+1}^n \tag{2.43}$$

and the positions are integrated using the second order Runge-Kutta method:

$$\underline{r}_{k+1}^n = \underline{r}_k^n + 0.5 \begin{pmatrix} \dfrac{1}{M+h} & 0 & 0 \\[2ex] 0 & \dfrac{1}{(N+h)\cos\varphi} & 0 \\[2ex] 0 & 0 & -1 \end{pmatrix} (\underline{v}_k^n + \underline{v}_{k+1}^n)\Delta t \tag{2.44}$$

where M and N are the radii of curvature in the meridian and prime vertical, respectively.

Figure 2.5 summarizes the overall navigation frame INS mechanization described in this section.
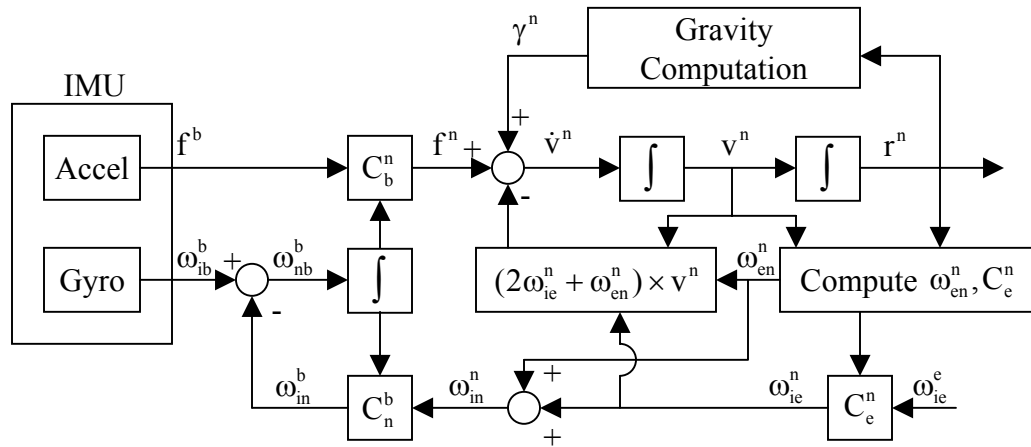
Figure 2.5: The navigation frame INS mechanization

Chapter 3

Development of INS/GPS Integration

Kalman Filter

In this chapter the error dynamics equations of inertial navigation systems will be derived

based on perturbation analysis. The nine-state INS/GPS integration Kalman filter will then

be built using the error dynamics equations. Several issues in implementing the Kalman

filter are also discussed in detail, such as correcting the lever-arm effect, resolving the GPS

and IMU measurement time difference, and the feedback/feedforward method.

3.1 Perturbation Analysis

The error analysis utilizes perturbation methods to linearize the nonlinear system differential equations (Britting, 1971, p. 20). For example, the perturbation of the position, velocity, attitude DCM, and gravity can be expressed as

$$\hat{\underline{r}}^n = \underline{r}^n + \delta\underline{r}^n \tag{3.1}$$

$$\hat{\underline{v}}^n = \underline{v}^n + \delta\underline{v}^n \tag{3.2}$$

$$\hat{C}_b^n = (I - E^n)C_b^n \tag{3.3}$$

$$\underline{\gamma}^n = \underline{g}^n + \delta\underline{g}^n \tag{3.4}$$

where $\underline{\gamma}$ denotes the normal gravity vector and E^n is the skew symmetric (or cross product) form of the attitude errors

$$E^n = (\underline{\epsilon}^n \times) = \begin{pmatrix} 0 & -\epsilon_D & \epsilon_E \\ \epsilon_D & 0 & -\epsilon_N \\ -\epsilon_E & \epsilon_N & 0 \end{pmatrix} \tag{3.5}$$

and $\hat{}$ and δ denote computed values and errors, respectively. The derivation of Eq. (3.3) is dealt with in Britting (1971, p. 21) as a transformation with an explicit orthogonality constraint.

3.2 Position Error Dynamics

The linearized position error dynamics can be obtained by perturbing Eq. (2.17), the dynamics equations for the geodetic positions. Since the position dynamics equations are functions of position and velocity, the position error dynamics equations can be obtained using the partial derivatives:

$$\delta \underline{\dot{r}}^n = F_{rr} \delta \underline{r}^n + F_{rv} \delta \underline{v}^n \tag{3.6}$$

where

$$
F_{rr} = \begin{pmatrix}
\dfrac{\partial \dot{\varphi}}{\partial \varphi} & \dfrac{\partial \dot{\varphi}}{\partial \lambda} & \dfrac{\partial \dot{\varphi}}{\partial h} \\[2mm]
\dfrac{\partial \dot{\lambda}}{\partial \varphi} & \dfrac{\partial \dot{\lambda}}{\partial \lambda} & \dfrac{\partial \dot{\lambda}}{\partial h} \\[2mm]
\dfrac{\partial \dot{h}}{\partial \varphi} & \dfrac{\partial \dot{h}}{\partial \lambda} & \dfrac{\partial \dot{h}}{\partial h}
\end{pmatrix}
= \begin{pmatrix}
0 & 0 & \dfrac{-v_N}{(M+h)^2} \\[2mm]
\dfrac{v_E \sin \varphi}{(N+h) \cos^2 \varphi} & 0 & \dfrac{-v_E}{(N+h)^2 \cos \varphi} \\[2mm]
0 & 0 & 0
\end{pmatrix}
$$

$$
F_{rv} = \begin{pmatrix}
\dfrac{\partial \dot{\varphi}}{\partial v_N} & \dfrac{\partial \dot{\varphi}}{\partial v_E} & \dfrac{\partial \dot{\varphi}}{\partial v_D} \\[2mm]
\dfrac{\partial \dot{\lambda}}{\partial v_N} & \dfrac{\partial \dot{\lambda}}{\partial v_E} & \dfrac{\partial \dot{\lambda}}{\partial v_D} \\[2mm]
\dfrac{\partial \dot{h}}{\partial v_N} & \dfrac{\partial \dot{h}}{\partial v_E} & \dfrac{\partial \dot{h}}{\partial v_D}
\end{pmatrix}
= \begin{pmatrix}
\dfrac{1}{M+h} & 0 & 0 \\[2mm]
0 & \dfrac{1}{(N+h) \cos \varphi} & 0 \\[2mm]
0 & 0 & -1
\end{pmatrix}
$$

and M, N are radii of curvature in the meridian and prime vertical, and are considered as constants.

3.3 Velocity Error Dynamics

Referring to Eq. (2.24), the computed version of the velocity dynamics equation can be expressed as

$$\hat{\dot{\underline{v}}}^n = \hat{C}_b^n \tilde{\underline{f}}^b - (2\hat{\underline{\omega}}_{ie}^n + \hat{\underline{\omega}}_{en}^n) \times \hat{\underline{v}}^n + \underline{\gamma}^n \tag{3.7}$$

Perturbing the above equation yields

$$\dot{\underline{v}}^n + \delta\dot{\underline{v}}^n = (I - E^n)C_b^n(\underline{f}^b + \delta\underline{f}^b)$$
$$- (2\underline{\omega}_{ie}^n + \underline{\omega}_{en}^n + 2\delta\underline{\omega}_{ie}^n + \delta\underline{\omega}_{en}^n) \times (\underline{v}^n + \delta\underline{v}^n) + \underline{g}^n + \delta\underline{g}^n \tag{3.8}$$

Collecting the first order terms, the above equation can be reduced to

$$\delta\dot{\underline{v}}^n = -(2\delta\underline{\omega}_{ie}^n + \delta\underline{\omega}_{en}^n) \times \underline{v}^n + \delta\underline{g}^n$$
$$- (2\underline{\omega}_{ie}^n + \underline{\omega}_{en}^n) \times \delta\underline{v}^n - \underline{\epsilon}^n \times \underline{f}^n + C_b^n \delta\underline{f}^b$$
$$= \underline{v}^n \times (2\delta\underline{\omega}_{ie}^n + \delta\underline{\omega}_{en}^n) + \delta\underline{g}^n$$
$$- (2\underline{\omega}_{ie}^n + \underline{\omega}_{en}^n) \times \delta\underline{v}^n + \underline{f}^n \times \underline{\epsilon}^n + C_b^n \delta\underline{f}^b \tag{3.9}$$

where the first and second terms on the right hand side can be developed into functions of position and velocity errors. Referring to Eq. (2.14),

$$2\underline{\omega}_{ie}^{n} + \underline{\omega}_{en}^{n} = \begin{pmatrix} 2\omega_{e}\cos\varphi + \dfrac{v_{E}}{N+h} \\[2ex] \dfrac{-v_{N}}{M+h} \\[2ex] -2\omega_{e}\sin\varphi - \dfrac{v_{E}\tan\varphi}{N+h} \end{pmatrix}. \tag{3.10}$$

Perturbing the above equation yields

$$2\delta\underline{\omega}_{ie}^{n} + \delta\underline{\omega}_{en}^{n} = \delta\Omega_{r}\delta\underline{r}^{n} + \delta\Omega_{v}\delta\underline{v}^{n} \tag{3.11}$$

where

$$\delta\Omega_{r} = \left(\begin{array}{c|c|c} -2\omega_{e}\sin\varphi & 0 & \dfrac{-v_{E}}{(N+h)^{2}} \\ \hline 0 & 0 & \dfrac{v_{N}}{(M+h)^{2}} \\ \hline -2\omega_{e}\cos\varphi - \dfrac{v_{E}}{(N+h)\cos^{2}\varphi} & 0 & \dfrac{v_{E}\tan\varphi}{(N+h)^{2}} \end{array} \right) \tag{3.12}$$

and

$$\delta\Omega_{v} = \begin{pmatrix} 0 & \dfrac{1}{N+h} & 0 \\[2ex] \dfrac{-1}{M+h} & 0 & 0 \\[2ex] 0 & \dfrac{-\tan\varphi}{N+h} & 0 \end{pmatrix}. \tag{3.13}$$

Using Eq. (3.11), the first term on the right hand side of Eq. (3.9) can be developed into the functions of the position and velocity errors

$$
\underline{v}^n \times (2\delta\underline{\omega}_{ie}^n + \delta\underline{\omega}_{en}^n) = (\underline{v}^n\times)(\delta\Omega_r\delta\underline{r}^n + \delta\Omega_v\delta\underline{v}^n)
$$
$$
= (\underline{v}^n\times)\delta\Omega_r\delta\underline{r}^n + (\underline{v}^n\times)\delta\Omega_v\delta\underline{v}^n \tag{3.14}
$$

Completing the algebra, we can get

$$
(\underline{v}^n\times)\delta\Omega_r = \left(\begin{array}{c|c|c}
\begin{array}{c} -2v_E\omega_e\cos\varphi \\ -\dfrac{v_E^2}{(N+h)\cos^2\varphi} \end{array} & 0 & \dfrac{-v_Nv_D}{(M+h)^2}+\dfrac{v_E^2\tan\varphi}{(N+h)^2} \\ \hline
\begin{array}{c} 2\omega_e(v_N\cos\varphi-v_D\sin\varphi) \\ +\dfrac{v_Ev_N}{(N+h)\cos^2\varphi} \end{array} & 0 & \dfrac{-v_Ev_D}{(N+h)^2}-\dfrac{v_Nv_E\tan\varphi}{(N+h)^2} \\ \hline
2v_E\omega_e\sin\varphi & 0 & \dfrac{v_E^2}{(N+h)^2}+\dfrac{v_N^2}{(M+h)^2}
\end{array}\right) \tag{3.15}
$$

$$
(\underline{v}^n\times)\delta\Omega_v = \left(\begin{array}{ccc}
\dfrac{v_D}{M+h} & \dfrac{-v_E\tan\varphi}{N+h} & 0 \\
0 & \dfrac{v_D}{N+h}+\dfrac{v_N\tan\varphi}{N+h} & 0 \\
\dfrac{-v_N}{M+h} & \dfrac{-v_E}{N+h} & 0
\end{array}\right) \tag{3.16}
$$

The gravity vector in the navigation frame, $\underline{g}^n$, is approximated by the normal gravity vector $(\ 0 \quad 0 \quad \gamma\ )^T$, and γ varies with altitude. Let us assume a spherical Earth model and the following simplified inverse square gravity model (Rogers, 2000, p. 70)

$$
\gamma = \gamma_0\left(\frac{R}{R+h}\right)^2, \tag{3.17}
$$

where γ_0 is the normal gravity at $h = 0$, and $R = \sqrt{MN}$. Perturbing the upper equation yields

$$\delta\gamma = -2\left(\frac{\gamma}{R+h}\right)\delta h \tag{3.18}$$

Using Eq. (3.10) $\sim$ (3.18), the velocity error dynamics equation Eq. (3.9) can be rewritten as

$$\delta\underline{\dot{v}}^n = F_{vr}\delta\underline{r}^n + F_{vv}\delta\underline{v}^n + (\underline{f}^n\times)\underline{\epsilon}^n + C_b^n\delta\underline{f}^b \tag{3.19}$$

where

$$
F_{vr} = \left(
\begin{array}{c|c|c}
\begin{array}{c} -2v_E\omega_e\cos\varphi \\ -\dfrac{v_E^2}{(N+h)\cos^2\varphi} \end{array} & 0 & \dfrac{-v_Nv_D}{(M+h)^2} + \dfrac{v_E^2\tan\varphi}{(N+h)^2} \\
\hline
\begin{array}{c} 2\omega_e(v_N\cos\varphi - v_D\sin\varphi) \\ +\dfrac{v_Ev_N}{(N+h)\cos^2\varphi} \end{array} & 0 & \dfrac{-v_Ev_D}{(N+h)^2} - \dfrac{v_Nv_E\tan\varphi}{(N+h)^2} \\
\hline
2v_E\omega_e\sin\varphi & 0 & \begin{array}{c} \dfrac{v_E^2}{(N+h)^2} + \dfrac{v_N^2}{(M+h)^2} \\ -2\gamma/(R+h) \end{array}
\end{array}
\right) \tag{3.20}
$$

$$
F_{vv} = \left(
\begin{array}{c|c|c}
\dfrac{v_D}{M+h} & \begin{array}{c} -2\omega_e\sin\varphi \\ -2\dfrac{v_E\tan\varphi}{N+h} \end{array} & \dfrac{v_N}{M+h} \\
\hline
\begin{array}{c} 2\omega_e\sin\varphi \\ +\dfrac{v_E\tan\varphi}{N+h} \end{array} & \dfrac{v_D + v_N\tan\varphi}{N+h} & 2\omega_e\cos\varphi + \dfrac{v_E}{N+h} \\
\hline
-2\dfrac{v_N}{M+h} & \begin{array}{c} -2\omega_e\cos\varphi \\ -2\dfrac{v_E}{N+h} \end{array} & 0
\end{array}
\right) \tag{3.21}
$$

3.4 Attitude Error Dynamics

The computed version, i.e. the output from the INS mechanization, of Eq. (2.25) can be expressed as

$$\dot{\hat{C}}_b^n = \hat{C}_b^n(\hat{\Omega}_{ib}^b - \hat{\Omega}_{in}^b). \tag{3.22}$$

Equating the derivative of Eq. (3.3) to Eq. (3.22) gives

$$
\begin{aligned}
-\dot{E}^n C_b^n + (I - E^n)\dot{C}_b^n &= (I - E^n)C_b^n(\Omega_{ib}^b - \Omega_{in}^b + \delta\Omega_{ib}^b - \delta\Omega_{in}^b) \\
&= (I - E^n)C_b^n(\Omega_{ib}^b - \Omega_{in}^b) + (I - E^n)C_b^n(\delta\Omega_{ib}^b - \delta\Omega_{in}^b) \\
&= (I - E^n)C_b^n\Omega_{nb}^b + (I - E^n)C_b^n(\delta\Omega_{ib}^b - \delta\Omega_{in}^b)
\end{aligned}
$$

Hence, the above equation can be reduced to

$$-\dot{E}^n C_b^n = (I - E^n)C_b^n(\delta\Omega_{ib}^b - \delta\Omega_{in}^b). \tag{3.23}$$

Collecting the first order terms, Eq. (3.23) can be rewritten as

$$\dot{E}^n = -C_b^n(\delta\Omega_{ib}^b - \delta\Omega_{in}^b)C_n^b, \tag{3.24}$$

or in vector form

$$\dot{\underline{\epsilon}}^n = -C_b^n(\delta\underline{\omega}_{ib}^b - \delta\underline{\omega}_{in}^b) \tag{3.25}$$

To get the error equation for $\delta\underline{\omega}_{in}^b$, let us start with $\hat{\underline{\omega}}_{in}^b = \hat{C}_n^b \hat{\underline{\omega}}_{in}^n$, which can be expanded into

$$\underline{\omega}_{in}^b + \delta\underline{\omega}_{in}^b = C_n^b(I + E^n)(\underline{\omega}_{in}^n + \delta\underline{\omega}_{in}^n).$$

Writing to the first order terms,

$$\delta\underline{\omega}_{in}^b = C_n^b(\delta\underline{\omega}_{in}^n + E^n\underline{\omega}_{in}^n) = C_n^b\left[\delta\underline{\omega}_{in}^n + (\underline{\epsilon}^n\times)\underline{\omega}_{in}^n\right] \tag{3.26}$$

Substituting Eq. (3.26) into Eq. (3.25),

$$\begin{aligned}
\underline{\dot{\epsilon}}^n &= \delta\underline{\omega}_{in}^n + (\underline{\epsilon}^n\times)\underline{\omega}_{in}^n - C_b^n\delta\underline{\omega}_{ib}^b \\
&= \delta\underline{\omega}_{in}^n - (\underline{\omega}_{in}^n\times)\underline{\epsilon}^n - C_b^n\delta\underline{\omega}_{ib}^b.
\end{aligned} \tag{3.27}$$

The next procedure to follow is expanding the first term on the right hand side into the position and velocity error terms explicitly. Referring to Eq. (2.14) and (3.11), the attitude error dynamics equations can be rewritten as

$$\underline{\dot{\epsilon}}^n = F_{er}\delta\underline{r}^n + F_{ev}\delta\underline{v}^n - (\underline{\omega}_{in}^n\times)\underline{\epsilon}^n - C_b^n\delta\underline{\omega}_{ib}^b, \tag{3.28}$$

where

$$F_{er} = \begin{pmatrix} -\omega_e \sin\varphi & 0 & \dfrac{-v_E}{(N+h)^2} \\[2.5ex] 0 & 0 & \dfrac{v_N}{(M+h)^2} \\[2.5ex] -\omega_e \cos\varphi - \dfrac{v_E}{(N+h)\cos^2\varphi} & 0 & \dfrac{v_E \tan\varphi}{(N+h)^2} \end{pmatrix} \tag{3.29}$$

$$F_{ev} = \begin{pmatrix} 0 & \dfrac{1}{N+h} & 0 \\[2.5ex] \dfrac{-1}{M+h} & 0 & 0 \\[2.5ex] 0 & \dfrac{-\tan\varphi}{N+h} & 0 \end{pmatrix} \tag{3.30}$$

3.5 Implementation of the INS/GPS Kalman Filter

A continuous system equations can be constructed by augmenting Eq. (3.6), (3.19), and (3.28) as follows:

$$\dot{\underline{x}} = F\underline{x} + G\underline{u}, \tag{3.31}$$

where F is the dynamics matrix, $\underline{x}$ is the state vector, G is a design matrix, $\underline{u}$ is the forcing vector function:

$$F = \begin{pmatrix} F_{rr} & F_{rv} & 0 \\ F_{vr} & F_{vv} & (\underline{f}^n\times) \\ F_{er} & F_{ev} & -(\underline{\omega}_{in}^n\times) \end{pmatrix} \qquad \underline{x} = \begin{pmatrix} \delta\underline{r}^n \\ \delta\underline{v}^n \\ \underline{\epsilon}^n \end{pmatrix}$$

$$G = \begin{pmatrix} 0 & 0 \\ C_b^n & 0 \\ 0 & -C_b^n \end{pmatrix} \qquad \underline{u} = \begin{pmatrix} \delta \underline{f}^b \\ \delta \underline{\omega}_{ib}^b \end{pmatrix}$$

The elements of $\underline{u}$ are white noise whose covariance matrix is given by

$$E[\underline{u}(t)\underline{u}(\tau)^T] = Q(t)\delta(t-\tau) \tag{3.32}$$

where the operator δ denotes the Dirac delta function whose unit is 1/time (Gelb *et al.*, 1974, p. 74–75). Q is called the spectral density matrix and has the form

$$Q = diag(\ \sigma_{ax}^2 \quad \sigma_{ay}^2 \quad \sigma_{az}^2 \quad \sigma_{\omega x}^2 \quad \sigma_{\omega y}^2 \quad \sigma_{\omega z}^2\ ) \tag{3.33}$$

where σ_a and σ_ω are standard deviations of accelerometers and gyroscopes, respectively.

Because strapdown inertial systems are usually implemented with high-rate sampled data, Eq. (3.31) is transformed to its discrete time form:

$$\underline{x}(t_{k+1}) = \Phi(t_{k+1}, t_k)\underline{x}(t_k) + \int_{t_k}^{t_{k+1}} \Phi(t_{k+1}, \tau)G(\tau)\underline{u}(\tau)d\tau \tag{3.34}$$

or in abbreviated notation

$$\underline{x}_{k+1} = \Phi_k \underline{x}_k + \underline{w}_k \tag{3.35}$$

where Φ_k is the state transition matrix, and $\underline{w}_k$ is the driven response at t_{k+1} due to the presence of the input white noise during the time interval (t_k, t_{k+1}) (Brown and Hwang, 1992, p. 220). Because a white sequence is a sequence of zero–mean random variables that are uncorrelated timewise, the covariance matrix associated with $\underline{w}_k$ is (Brown and Hwang, 1992, p. 219)

$$E[\underline{w}_k \underline{w}_i^T] = \begin{cases} Q_k, & i = k \\ \\ 0, & i \neq k \end{cases} \tag{3.36}$$

The analytical method to find the state transition matrix is

$$\Phi_k = \mathcal{L}^{-1}\left[(sI - F)^{-1}\right] \tag{3.37}$$

where $\mathcal{L}^{-1}$ represents the inverse Laplace transform and s is the Laplace transform parameter. However, for the implementation of INS, because the sampling time interval $\Delta t = t_{k+1} - t_k$ is very small, following simple numerical approximation is preferred:

$$\Phi_k = \exp(F\Delta t) \approx I + F\Delta t \tag{3.38}$$

The equation for Q_k has the following form (Brown and Hwang, 1992, p. 220):

$$Q_k = E[\underline{w}_k \underline{w}_k^T]$$

$$= E\left\{\left[\int_{t_k}^{t_{k+1}} \Phi(t_{k+1},\xi)G(\xi)\underline{u}(\xi)d\xi\right]\left[\int_{t_k}^{t_{k+1}} \Phi(t_{k+1},\eta)G(\eta)\underline{u}(\eta)d\eta\right]^T\right\}$$

$$= \int_{t_k}^{t_{k+1}}\int_{t_k}^{t_{k+1}} \Phi(t_{k+1},\xi)G(\xi)E[\underline{u}(\xi)\underline{u}^T(\eta)]G^T(\eta)\Phi^T(t_{k+1},\eta)d\xi d\eta \tag{3.39}$$

A common approximate solution to Eq. (3.39) is given as

$$Q_k \approx GQG^T\Delta t \tag{3.40}$$

This approximation does not account for any of the correlations between the components of the driving noise $\underline{w}_k$ that develop over the course of a sampling period because of the integration of the continuous-time driving noise through the state dynamics (Farrell and Barth, 1998, p. 85). Therefore, in this research Q_k is calculated using the first order approximation of the transition matrix, i.e. Eq. (3.38), as

$$Q_k \approx \Phi_k GQG^T\Phi_k^T\Delta t \tag{3.41}$$

If the norm of Q_k is larger than the real one, the Kalman filter trusts the measurements more than the system. Then, the resulting estimates will be noisy due to the free passage of the measurement noise. However, the estimate does not have time lag (Salychev, 1998, p. 198). If the norm of Q_k is smaller than the real one, the time lag will show up. When the norm of Q_k is much smaller than the real one, the filter diverges, which may result in numerical instabilities. Hence, for low cost inertial systems, Q_k must be selected pessimistically so that the trajectory can follow that of GPS; especially, the elements corresponding to δf_z

should be large enough so that they can account for the uncertainties in gravity as well as sensor imperfection. In this thesis, the elements of Q_k were increased until the filter was stabilized and the trajectory could follow that of the GPS. Adaptive calculation methods can be applied to help in the tuning of Q_k, for more detail see for instance Salychev (1998) and Mohamed (1999).

The derivation of the Kalman filter – a recursive, unbiased and minimum-variance estimator – starts from the random process model, i.e. Eq. (3.35), and the following observation equations

$$\underline{z}_k = H_k \underline{x}_k + \underline{e}_k, \tag{3.42}$$

which express the vector measurement, $\underline{z}_k$, at time t_k as a linear combination of the state vector, $\underline{x}_k$, plus a random measurement error, $\underline{e}_k$ (Gelb *et al.*, 1974; Brown and Hwang, 1992). The covariance matrices for the $\underline{w}_k$ and $\underline{e}_k$ are given by

$$E[\underline{e}_k \underline{e}_i^T] = \begin{cases} R_k, & i = k \\ 0, & i \neq k \end{cases} \tag{3.43}$$

$$E[\underline{w}_k \underline{e}_i^T] = 0, \quad \forall i, k \tag{3.44}$$

The implementation of the Kalman filter can be divided into two stages, the update and prediction. In the former, the Kalman gain, K_k, is computed first, and then the state and

the error covariance are updated using the prior estimate, $\hat{\underline{x}}_k^-$, and its error covariance, P_k^-:

$$K_k \;=\; P_k^- H_k^T (H_k P_k^- H_k^T + R_k)^{-1} \tag{3.45}$$

$$\hat{\underline{x}}_k \;=\; \hat{\underline{x}}_k^- + K_k(\underline{z}_k - H_k \hat{\underline{x}}_k^-) \tag{3.46}$$

$$P_k \;=\; (I - K_k H_k) P_k^- \tag{3.47}$$

In the prediction stage, the estimate and its error covariance are projected ahead:

$$\hat{\underline{x}}_{k+1}^- \;=\; \Phi_k \hat{\underline{x}}_k \tag{3.48}$$

$$P_{k+1}^- \;=\; \Phi_k P_k \Phi_k^T + Q_k \tag{3.49}$$

The position and velocity from GPS can be considered as measurements. The straightforward formulation of the measurement equation can be written as

$$\underline{z}_k = \begin{pmatrix} \dfrac{r_{INS}^n - r_{GPS}^n}{v_{INS}^n - v_{GPS}^n} \end{pmatrix} = \begin{pmatrix} \varphi_{INS} - \varphi_{GPS} \\ \lambda_{INS} - \lambda_{GPS} \\ \dfrac{h_{INS} - h_{GPS}}{v_{INS}^n - v_{GPS}^n} \end{pmatrix} \qquad H_k = \left(\begin{array}{c|c|c} I_{3\times3} & 0_{3\times3} & 0_{3\times3} \\ \hline 0_{3\times3} & I_{3\times3} & 0_{3\times3} \end{array} \right) \tag{3.50}$$

However, this approach causes numerical instabilities in calculating $(H_k P_k^- H_k^T + R_k)^{-1}$ for the Kalman gain, K_k, because φ and λ are in radians and therefore they are very small

values. This problem can be resolved if the first and second rows are multiplied by $(M + h)$ and $(N + h)\cos\varphi$, respectively. Hence, the measurement equation will take the form:

$$
\underline{z}_k = \begin{pmatrix} (M+h)(\varphi_{INS} - \varphi_{GPS}) \\ (N+h)\cos\varphi(\lambda_{INS} - \lambda_{GPS}) \\ h_{INS} - h_{GPS} \\ \hline \underline{v}^n_{INS} - \underline{v}^n_{GPS} \end{pmatrix}
$$

$$
H_k = \left(\begin{array}{ccc|c|c} (M+h) & 0 & 0 & & \\ 0 & (N+h)\cos\varphi & 0 & 0_{3\times3} & 0_{3\times3} \\ 0 & 0 & 1 & & \\ \hline & 0_{3\times3} & & I_{3\times3} & 0_{3\times3} \end{array} \right)
\tag{3.51}
$$

and the following measurement noise matrix will be used

$$
R_k = diag(\begin{array}{cccccc} \sigma_\varphi^2 & \sigma_\lambda^2 & \sigma_h^2 & \sigma_{vn}^2 & \sigma_{ve}^2 & \sigma_{vd}^2 \end{array})
\tag{3.52}
$$

which can be obtained from GPS processing.

To start a Kalman filter, the initial estimation uncertainty standard deviations must be given first. If an IMU is initialized in stationary mode, the position uncertainty will be that of the GPS solution and the velocity uncertainty will be almost zero. The attitude uncertainty is totally dependent on the accelerometer and gyroscope biases. If the biases can be estimated,

the attitude uncertainty can also be reduce. If the biases are not estimated, the attitude uncertainty can be obtained using equations (4.49), (4.50), and (4.51).

As shown in Figure 3.1, the GPS and IMU measurements are usually made in different time. So, the IMU's position and velocity can be interpolated using the data before and after the GPS measurement is made to compose the vector $\underline{z}_k$. Let's assume that IMU measurements are made at t_{k-1} and t_k, and the GPS measurement is mate at t_{GPS}. Then, following linear interpolation equations can be applied to get the position and veocity of IMU at the GPS measurement time:

$$
\begin{aligned}
\underline{r}^n(t_{GPS}) &= \underline{r}^n(t_{k-1}) + \frac{\underline{r}^n(t_k) - \underline{r}^n(t_{k-1})}{t_k - t_{k-1}}(t_{GPS} - t_{k-1}) \\
&= \frac{t_k - t_{GPS}}{t_k - t_{k-1}}\underline{r}^n(t_{k-1}) + \frac{t_{GPS} - t_{k-1}}{t_k - t_{k-1}}\underline{r}^n(t_k) \tag{3.53}
\end{aligned}
$$

$$
\underline{v}^n(t_{GPS}) = \frac{t_k - t_{GPS}}{t_k - t_{k-1}}\underline{v}^n(t_{k-1}) + \frac{t_{GPS} - t_{k-1}}{t_k - t_{k-1}}\underline{v}^n(t_k) \tag{3.54}
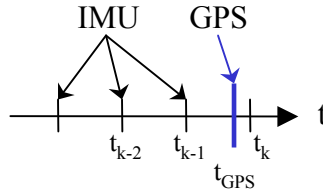$$

Figure 3.1: GPS and IMU measurement time

For high dynamic applications, higher order interpolation is needed. For example, the La-

grange interpolation equation can be used:(Conte and de Boor, 1980, p. 38)

$$\underline{r}^n(t_{GPS}) \quad = \quad \sum_{i=k-m-1}^{k+m} \underline{r}^n(t_i) \prod_{\substack{j=k-m-1 \\ j \neq i}}^{k+m} \frac{t_{GPS} - t_j}{t_i - t_j} \tag{3.55}$$

$$\underline{v}^n(t_{GPS}) \quad = \quad \sum_{i=k-m-1}^{k+m} \underline{v}^n(t_i) \prod_{\substack{j=k-m-1 \\ j \neq i}}^{k+m} \frac{t_{GPS} - t_j}{t_i - t_j} \tag{3.56}$$

where $2m + 1$ is the order of interpolation. When $m = 0$, Eq. (3.55) and (3.56) are identical

to Eq. (3.53) and (3.54), respectively.

Since both sensors cannot be installed at the same place in the host vehicle as shown in

Figure 3.2, the position and velocity of the IMU are different from those of the GPS. This

is called the lever-arm effect. The lever-arm correction for the position and velocity can be

written as:

$$\underline{r}^n_{IMU} \quad = \quad \underline{r}^n_{GPS} - \begin{pmatrix} \dfrac{1}{M+h} & 0 & 0 \\[2ex] 0 & \dfrac{1}{(N+h)\cos\varphi} & 0 \\[2ex] 0 & 0 & -1 \end{pmatrix} C^n_b \Delta\underline{r}^b \tag{3.57}$$

$$\underline{v}^n_{IMU} \quad = \quad \underline{v}^n_{GPS} - C^n_b \Omega^b_{nb} \Delta\underline{r}^b$$

$$= \quad \underline{v}^n_{GPS} - C^n_b (\Omega^b_{ni} + \Omega^b_{ib}) \Delta\underline{r}^b$$

$$= \quad \underline{v}^n_{GPS} + C^n_b \Omega^b_{in} \Delta\underline{r}^b - C^n_b \Omega^b_{ib} \Delta\underline{r}^b$$

$$= \quad \underline{v}^n_{GPS} + C^n_b \Omega^b_{in} C^b_n C^n_b \Delta\underline{r}^b - C^n_b \Omega^b_{ib} \Delta\underline{r}^b$$

$$= \quad \underline{v}^n_{GPS} + (\Omega^n_{ie} + \Omega^n_{en}) C^n_b \Delta\underline{r}^b - C^n_b \Omega^b_{ib} \Delta\underline{r}^b, \tag{3.58}$$

where $\Delta\underline{r}^b$ is the offset vector of the GPS antenna from the centre of the IMU in the body frame.
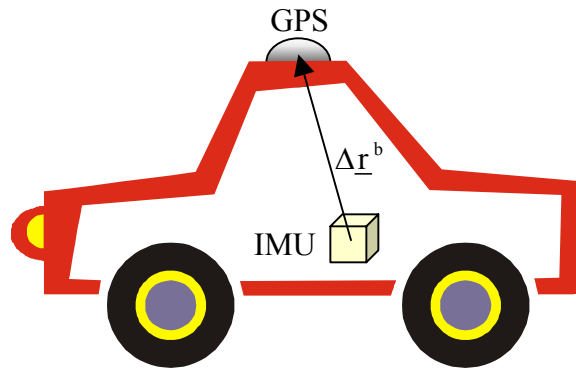
Figure 3.2: Lever–arm effect

The estimated errors in the navigation components are fed back to the mechanization, see Figure 3.4, or fed forward to the output, see Figure 3.3. In the feedforward method, the inertial system operates as if there was no aiding: it is unaware of the existence of the filter or the external data (Maybeck, 1994, p. 296). The disadvantage of the feedforward method is that the mechanization can experience unbounded error growth, which makes unbounded error observations delivered to the Kalman filter. This causes a problem to the linear filter since only small errors are allowed due to the linearization process (Sukkarieh, 2000, p. 21). Therefore, the feedback method is optimal for low cost INSs.
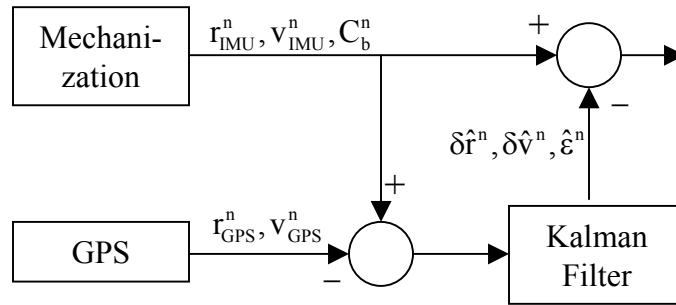
Figure 3.3: The feedforward method
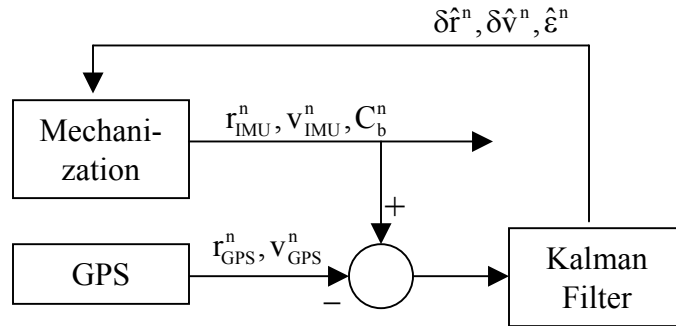
Figure 3.4: The feedback method

The feedback of the position and velocity vectors can be easily obtained from Eq. (3.1) and

Eq. (3.2)

$$\underline{r}^n = \hat{\underline{r}}^n - \delta\underline{r}^n, \tag{3.59}$$

$$\underline{v}^n = \hat{\underline{v}}^n - \delta\underline{v}^n. \tag{3.60}$$

The following characteristic holds to the first order attitude errors (Farrell and Barth, 1998, p. 200):

$$(I - E^n)^{-1} = (I + E^n) \tag{3.61}$$

Hence, Eq. (3.3) can be manipulated to yield the DCM attitude feedback:

$$C_b^n = (I + E^n)\hat{C}_b^n \tag{3.62}$$

After feedback is done the error state vector should be set to zero. Because, for the nine-state INS/GPS integration Kalman filter, the state vector is zero until the next measurements are made, if feedback is made every time measurements take place, the state prediction, Eq. (3.48), does not need to be implemented at all and Eq. (3.46) reduces to

$$\hat{\underline{x}}_k = K_k \underline{z}_k. \tag{3.63}$$

Chapter 4

Accuracy Improvement of Low Cost INS/GPS

In this chapter, various ways to improve the accuracy of low cost inertial systems will be discussed. After discussing some characteristics that a field calibration method should have, a special calibration method developed by Shin and El-Sheimy (2002) and its implication will be analyzed. Then, the velocity matching alignment technique, with which the IMU can be aligned while moving, will be introduced. The use of non-holonomic constraints as measurements in the Kalman filter will be developed. Finally, the way to deal with the zero velocity measurements for low cost inertial systems will be discussed.

4.1   Field Calibration Methods

Calibration of inertial instruments is needed because the outputs of the instruments are corrupted by errors. Chatfield (1997, p. 79) defined calibration as the process of comparing instrument outputs with known reference information and determining coefficients that force the output to agree with the reference information over a range of output values. Calibration parameters to be determined can change according to the specific technology applied to the IMU. To accurately determine all parameters special calibration devices such as three-axial turn tables and estimation techniques are necessary.

Biases and scale factors are changing from switch-on to switch-on. Furthermore, for low cost IMUs, the variation ranges of the calibration parameters are much larger than those of the high performance ones. So, what lab calibration methods can do is very limited. Instead field calibration method should be applied for low cost IMUs. The following are some characteristics that a field calibration method should have: First, it should not take a long time for the calibration. Because biases of low cost IMUs can drift, the biases at the start of the calibration will be much different from those at the end of the calibration, if the calibration time gets too long. So, the field calibration should be applied even during a mission, if the mission lasts for long time. Second, the method should be easy to use in the field environment. So it should not be dependent on the attitude of the IMU. In other words, the calibration can also be done without aligning the IMU to the local level frame.

If rotations should be made, an automatic rotational frame would make the calibration procedure convenient.

For automotive-grade and consumer-grade IMUs, the stationary outputs of gyroscopes themselves can be considered as biases (Sukkarieh, 2000, p. 65). However, for the accelerometer calibration of all IMUs and for the gyroscope calibration of tactical-grade IMUs in the field, a different calibration method is needed. A new calibration method, which does not require the use of any laboratory facilities and therefore can be used as a field method, was introduced by Shin and El-Sheimy (2002). At first, the general bias, scale factor, and nonorthogonality model will be derived. Then, because it is hard to determine the nonorthogonalities in the field, the bias and scale factor model will be derived from the general model. The accelerometer calibration method is dependent on the reference gravity value. However, we can only use normal gravity values sometimes, especially for the calibration during a mission. Therefore, the sensitivity of the method to the reference gravity error will be analyzed. Since, the Earth's rotation rate is a very weak signal, only biases will be considered as the parameters for the gyroscope calibration.

4.1.1 Consideration of Nonorthogonality

All vectors in $\mathcal{R}^3$ space can be expressed as a linear combinations of the following three orthonormal vectors that correspond to the three orthogonal axes of accelerometers or gyro-

scopes of an IMU:

$$\underline{x} : (\begin{matrix} 1 & 0 & 0 \end{matrix})^T, \quad \underline{y} : (\begin{matrix} 0 & 1 & 0 \end{matrix})^T, \quad \underline{z} : (\begin{matrix} 0 & 0 & 1 \end{matrix})^T. \tag{4.1}$$

The values sensed by each of these axes can be expressed using the inner products of the measurement vector and the orthonormal vectors. For instance, the components of the gravity vector, $\underline{g} : (\begin{matrix} g_x & g_y & g_z \end{matrix})^T$, can be expressed as

$$g_x = \; < \underline{g}, \underline{x} > = \|\underline{g}\| \cos \alpha \tag{4.2}$$

$$g_y = \; < \underline{g}, \underline{y} > = \|\underline{g}\| \cos \beta \tag{4.3}$$

$$g_z = \; < \underline{g}, \underline{z} > = \|\underline{g}\| \cos \gamma \tag{4.4}$$

where, $<,>$ denotes the inner product and α, β, γ are, as shown in Figure 4.1, the angles between the gravity vector and the x, y, z axis, respectively. Then, the following characteristic holds regardless of the misalignment to the local-level frame and plays a fundamental role in this derivation:

$$g_x^2 + g_y^2 + g_z^2 = \|\underline{g}\|(\cos^2 \alpha + \cos^2 \beta + \cos^2 \gamma) = \|\underline{g}\| \tag{4.5}$$

In reality, the three axes of the accelerometers or gyroscopes of an IMU may not be perfectly orthogonal to each other. As shown in Figure 4.2, when the y-axis is rotated by the angle
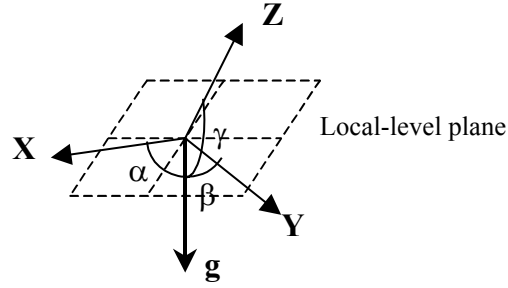
Figure 4.1: Misalignment to the local level frame

θ_{yz}, this rotated axis can be represented as following unit vector:

$$\underline{y}_1 : (\ -\sin\theta_{yz} \quad \cos\theta_{yz} \quad 0\ )^T = R_z(\theta_{yz})\underline{y}, \tag{4.6}$$

where R_z is the rotation matrix for a vector around z-axis

$$R_z(\theta_{yz}) = \begin{pmatrix} \cos\theta_{yz} & -\sin\theta_{yz} & 0 \\ \sin\theta_{yz} & \cos\theta_{yz} & 0 \\ 0 & 0 & 1 \end{pmatrix}.$$
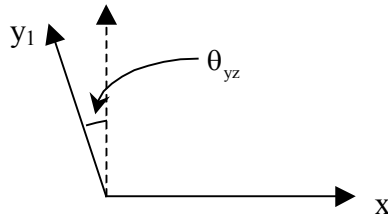
Figure 4.2: Nonorthogonality between x and y

In $\mathcal{R}^3$ space, the nonorthogonality of the z-axis, for example, can be expressed by successive two rotations, i.e. a rotation with respect to the x-axis by the angle, θ_{zx}, and a rotation

about the y-axis by the angle, θ_{zy}. This nonorthogonal z-axis can again be represented using the following unit vector

$$\underline{z}_1 : (\ \sin\theta_{zy} \quad -\sin\theta_{zx}\cos\theta_{zy} \quad \cos\theta_{zx}\cos\theta_{zy}\ )^T = R_x(\theta_{zx})R_y(\theta_{zy})\underline{z}. \tag{4.7}$$

where R_x and R_y are rotation matrices for a vector with respect to the x-axis and y-axis, respectively, and defined by

$$R_x(\theta_{zx}) = \begin{pmatrix} 1 & 0 & 0 \\ 0 & \cos\theta_{zx} & -\sin\theta_{zx} \\ 0 & \sin\theta_{zx} & \cos\theta_{zx} \end{pmatrix}, R_y(\theta_{zy}) = \begin{pmatrix} \cos\theta_{zy} & 0 & \sin\theta_{zy} \\ 0 & 1 & 0 \\ -\sin\theta_{zy} & 0 & \cos\theta_{zy} \end{pmatrix}$$
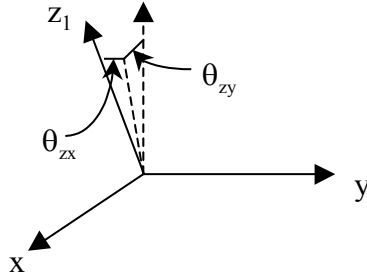
Figure 4.3: Nonorthogonality of z-axis to xy plane

Hence, considering nonorthogonalities of θ_{yz}, θ_{zx}, and θ_{zy}, all vectors in $\mathcal{R}^3$ space can be expressed as linear combinations of the following three vectors that correspond to three nonorthogonal axes of the accelerometers or gyroscopes of an IMU:

$$\underline{x}_1 \ : \ (\ 1 \quad 0 \quad 0\ )^T, \tag{4.8}$$

$$\underline{y}_1 \ : \ (\ -\sin\theta_{yz} \quad \cos\theta_{yz} \quad 0 \ )^T, \tag{4.9}$$

$$\underline{z}_1 \ : \ (\ \sin\theta_{zy} \quad -\sin\theta_{zx}\cos\theta_{zy} \quad \cos\theta_{zx}\cos\theta_{zy} \ )^T. \tag{4.10}$$

The values to be sensed by each of these nonorthogonal axes can be expressed using again the inner product, for instance for the gravity vector $\underline{g} : (g_x, g_y, g_z)$,

$$g_{x1} \ = \ < \underline{g}, \underline{x}_1 > = g_x, \tag{4.11}$$

$$g_{y1} \ = \ < \underline{g}, \underline{y}_1 > = -g_x\sin\theta_{gyz} + g_y\cos\theta_{gyz}, \tag{4.12}$$

$$g_{z1} \ = \ < \underline{g}, \underline{z}_1 > = g_x\sin\theta_{gzy} - g_y\sin\theta_{gzx}\cos\theta_{gzy} + g_z\cos\theta_{gzx}\cos\theta_{gzy}. \tag{4.13}$$

4.1.2 A New Calibration Method

The new calibration method makes use of the fact that regardless of the direction that the IMU axes are pointing, the total values sensed by the accelerometers and the gyroscopes in static mode should be equal to the gravity and the Earth's rotation rate, respectively. Taking biases, scale factors, and nonorthogonalities into account, the values to be measured by each of the axes as a result of the gravity vector $\underline{g}$ can be written as:

$$\ell_{gx} \ = \ b_{gx} + (1 + s_{gx})g_x, \tag{4.14}$$

$$\ell_{gy} \ = \ b_{gy} + (1 + s_{gy})(-g_x\sin\theta_{gyz} + g_y\cos\theta_{gyz}), \tag{4.15}$$

$$\ell_{gz} \ = \ b_{gz} + (1 + s_{gz})(g_x\sin\theta_{gzy}$$

$$-g_y \sin\theta_{gzx} \cos\theta_{gzy} + g_z \cos\theta_{gzx} \cos\theta_{gzy}) \tag{4.16}$$

where b and s represent bias and scale factor, respectively. Rearranging the upper equations we can obtain the true values for the gravity vector components:

$$g_x = \frac{\ell_{gx} - b_{gx}}{1 + s_{gx}} \tag{4.17}$$

$$g_y = \tan\theta_{gyz} \left(\frac{\ell_{gx} - b_{gx}}{1 + s_{gx}} \right) + \left(\frac{1}{\cos\theta_{gyz}} \right) \left(\frac{\ell_{gy} - b_{gy}}{1 + s_{gy}} \right) \tag{4.18}$$

$$g_z = \left(\tan\theta_{gzx} \tan\theta_{gyz} - \frac{\tan\theta_{gzy}}{\cos\theta_{gzx}} \right) \left(\frac{\ell_{gx} - b_{gx}}{1 + s_{gx}} \right)$$
$$+ \left(\frac{\tan\theta_{gzx}}{\cos\theta_{gyz}} \right) \left(\frac{\ell_{gy} - b_{gy}}{1 + s_{gy}} \right) + \left(\frac{1}{\cos\theta_{gzx} \cos\theta_{gzy}} \right) \left(\frac{\ell_{gz} - b_{gz}}{1 + s_{gz}} \right). \tag{4.19}$$

Since scale factors and nonorthogonalities cannot be calibrated with stationary measurements for gyroscopes, equations for gyroscopes will be

$$\omega_x = \ell_{\omega x} - b_{\omega x} \tag{4.20}$$

$$\omega_y = \ell_{\omega y} - b_{\omega y} \tag{4.21}$$

$$\omega_y = \ell_{\omega z} - b_{\omega z} \tag{4.22}$$

Using Eq. (4.17) $\sim$ (4.22), we can define a general mathematical model for the calibration of a triad of accelerometers by

$$f_g = g_x^2 + g_y^2 + g_z^2 - \|\underline{g}\|^2 = 0 \tag{4.23}$$

and for a triad of gyroscopes by

$$f_\omega = \omega_x^2 + \omega_y^2 + \omega_z^2 - \|\underline{\omega}_{ie}\|^2 = 0 \tag{4.24}$$

By substituting Eq. (4.17) $\sim$ (4.19) into (4.23) and (4.20) $\sim$ (4.22) into (4.24), following mathematical models can be obtained:

$$
\begin{aligned}
f_g &= \left[\frac{\ell_{gx} - b_{gx}}{1 + s_{gx}}\right]^2 + \left[\tan\theta_{gyz}\left(\frac{\ell_{gx} - b_{gx}}{1 + s_{gx}}\right) + \left(\frac{1}{\cos\theta_{gyz}}\right)\left(\frac{\ell_{gy} - b_{gy}}{1 + s_{gy}}\right)\right]^2 \\
&+ \left[\left(\tan\theta_{gzx}\tan\theta_{gyz} - \frac{\tan\theta_{gzy}}{\cos\theta_{gzx}}\right)\left(\frac{\ell_{gx} - b_{gx}}{1 + s_{gx}}\right)\right. \\
&+ \left(\frac{\tan\theta_{gzx}}{\cos\theta_{gyz}}\right)\left(\frac{\ell_{gy} - b_{gy}}{1 + s_{gy}}\right) \\
&+ \left.\left(\frac{1}{\cos\theta_{gzx}\cos\theta_{gzy}}\right)\left(\frac{\ell_{gz} - b_{gz}}{1 + s_{gz}}\right)\right]^2 - \|\underline{g}\|^2 = 0 \tag{4.25} \\
f_\omega &= (\ell_{\omega x} - b_{\omega x})^2 + (\ell_{\omega y} - b_{\omega y})^2 + (\ell_{\omega z} - b_{\omega z})^2 - \|\underline{\omega}_{ie}\|^2 = 0 \tag{4.26}
\end{aligned}
$$

Because it is hard to calibrate nonorthogonalities in the field, the bias and scale factor only model can be considered for accelerometers:

$$f_g = \left(\frac{\ell_{gx} - b_{gx}}{1 + s_{gx}}\right)^2 + \left(\frac{\ell_{gy} - b_{gy}}{1 + s_{gy}}\right)^2 + \left(\frac{\ell_{gz} - b_{gz}}{1 + s_{gz}}\right)^2 - \|\underline{g}\|^2 = 0 \tag{4.27}$$

4.1.3 Adjustment Computation

The implicit mathematical models, Eq. (4.25) $\sim$ (4.27), are implemented in adjustment procedures using the combined case least squares method with weighted parameters, for

details refer to Krakiwsky (1990):

$$A\hat{\underline{\delta}} + B\hat{\underline{r}} + \underline{w} = 0; \quad \hat{\underline{x}} = \underline{x} + \hat{\underline{\delta}}; \quad \hat{\underline{\ell}} = \underline{\ell} + \hat{\underline{r}} \tag{4.28}$$

For the bias, scale factor, and nonorthogonality model of accelerometers, the design matrices A and B are given by

$$A = \begin{pmatrix} \cdots & \cdots & \cdots & \cdots & \cdots & \cdots & \cdots & \cdots & \cdots \\ \dfrac{\partial f_g}{\partial b_{gx}} & \dfrac{\partial f_g}{\partial b_{gy}} & \dfrac{\partial f_g}{\partial b_{gz}} & \dfrac{\partial f_g}{\partial s_{gx}} & \dfrac{\partial f_g}{\partial s_{gy}} & \dfrac{\partial f_g}{\partial s_{gz}} & \dfrac{\partial f_g}{\partial \theta_{gyx}} & \dfrac{\partial f_g}{\partial \theta_{gzx}} & \dfrac{\partial f_g}{\partial \theta_{gzy}} \\ \cdots & \cdots & \cdots & \cdots & \cdots & \cdots & \cdots & \cdots & \cdots \end{pmatrix}$$

$$B = \begin{pmatrix} \cdots & \cdots & \cdots & 0 & 0 & 0 & 0 & 0 & 0 \\ 0 & 0 & 0 & \dfrac{\partial f_g}{\partial \ell_{gx}} & \dfrac{\partial f_g}{\partial \ell_{gy}} & \dfrac{\partial f_g}{\partial \ell_{gz}} & 0 & 0 & 0 \\ 0 & 0 & 0 & 0 & 0 & 0 & \cdots & \cdots & \cdots \end{pmatrix}$$

where

$$\frac{\partial f_g}{\partial b_{gx}} = -2\frac{g_x + g_y \tan\theta_{gyz} + g_z (\tan\theta_{gzx}\tan\theta_{gyz} - \tan\theta_{gzy}/\cos\theta_{gzx})}{1 + s_{gx}}$$

$$\frac{\partial f_g}{\partial b_{gy}} = -2\frac{g_y + g_z \tan\theta_{gzx}}{(1 + s_{gy})\cos\theta_{gyz}}$$

$$\frac{\partial f_g}{\partial b_{gz}} = -2\frac{g_z}{(1 + s_{gz})\cos\theta_{gzx}\cos\theta_{gzy}}$$

$$\frac{\partial f_g}{\partial s_{gx}} = -2(\ell_{gx} - b_{gx})\frac{g_x + g_y \tan\theta_{gyz} + g_z (\tan\theta_{gzx}\tan\theta_{gyz} - \tan\theta_{gzy}/\cos\theta_{gzx})}{(1 + s_{gx})^2}$$

$$\frac{\partial f_g}{\partial s_{gy}} = -2(\ell_{gy} - b_{gy})\frac{g_y + g_z \tan\theta_{gzx}}{(1 + s_{gy})^2 \cos\theta_{gyz}}$$

$$\frac{\partial f_g}{\partial s_{gz}} = -2(\ell_{gz} - b_{gz})\frac{g_z}{(1 + s_{gz})^2 \cos\theta_{gzx} \cos\theta_{gzy}}$$

$$\frac{\partial f_g}{\partial \theta_{gyz}} = 2(g_y + g_z \tan\theta_{gzx})\left[\frac{\ell_{gx} - b_{gx}}{(1 + s_{gx})\cos^2\theta_{gyz}} + \frac{(\ell_{gy} - b_{gy})\tan\theta_{gyz}}{1 + s_{gy}}\right]$$

$$\frac{\partial f_g}{\partial \theta_{gzx}} = 2g_x\left[\left(\frac{\tan\theta_{gyz}}{\cos^2\theta_{gzx}} - \tan\theta_{gzx}\tan\theta_{gzy}\right)\left(\frac{\ell_{gx} - b_{gx}}{1 + s_{gx}}\right)\right.$$
$$\left. + \frac{\ell_{gy} - b_{gy}}{\cos^2\theta_{gzx}\cos\theta_{gyz}(1 + s_{gy})} + \frac{\tan\theta_{gzx}(\ell_{gz} - b_{gz})}{\cos\theta_{gzy}(1 + s_{gz})}\right]$$

$$\frac{\partial f_g}{\partial \theta_{gzy}} = 2g_z\left[\frac{-(\ell_{gx} - b_{gx})}{\cos\theta_{gzx}\cos^2\theta_{gzy}(1 + s_{gx})} + \frac{\tan\theta_{gzy}(\ell_{gz} - b_{gz})}{\cos\theta_{gzx}(1 + s_{gz})}\right]$$

$$\frac{\partial f_g}{\partial \ell_{gx}} = 2\frac{g_x + g_y\tan\theta_{gyz} + g_z(\tan\theta_{gzx}\tan\theta_{gyz} - \tan\theta_{gzy}/\cos\theta_{gzx})}{1 + s_{gx}}$$

$$\frac{\partial f_g}{\partial \ell_{gy}} = 2\frac{g_y + g_z\tan\theta_{gzx}}{\cos\theta_{gyz}(1 + s_{gy})}$$

$$\frac{\partial f_g}{\partial \ell_{gz}} = 2\frac{g_z}{\cos\theta_{gzx}\cos\theta_{gzy}(1 + s_{gy})}$$

$\underline{\ell}$ is the vector of observations

$$\underline{\ell} = (\ \ldots\quad \ldots\quad \ldots\quad \ell_{gx}\quad \ell_{gy}\quad \ell_{gz}\quad \ldots\quad \ldots\quad \ldots\ )^T$$

$\underline{\hat{\delta}}$ is the correction vector

$$\underline{\hat{\delta}} = (\ \delta b_{gx}\quad \delta b_{gy}\quad \delta b_{gz}\quad \delta s_{gx}\quad \delta s_{gy}\quad \delta s_{gz}\quad \delta\theta_{gyz}\quad \delta\theta_{gzx}\quad \delta\theta_{gzy}\ )^T$$

$\underline{\hat{r}}$ is the vector of residuals

$$\underline{\hat{r}} = (\ \ldots\quad \ldots\quad \ldots\quad r_{gx}\quad r_{gy}\quad r_{gz}\quad \ldots\quad \ldots\quad \ldots\ )^T$$

and $\underline{w}$ is the misclosure vector

$$\underline{w} = (\quad \cdots \quad f_g(\underline{x}, \underline{\ell}) \quad \cdots \quad)^T$$

For the bias and scale factor model of accelerometers, the differences are

$$A \;=\; \begin{pmatrix} \cdots & \cdots & \cdots & \cdots & \cdots & \cdots \\[4pt] \dfrac{\partial f_g}{\partial b_{gx}} & \dfrac{\partial f_g}{\partial b_{gy}} & \dfrac{\partial f_g}{\partial b_{gz}} & \dfrac{\partial f_g}{\partial s_{gx}} & \dfrac{\partial f_g}{\partial s_{gy}} & \dfrac{\partial f_g}{\partial s_{gz}} \\[10pt] \cdots & \cdots & \cdots & \cdots & \cdots & \cdots \end{pmatrix}$$

$$\hat{\underline{\delta}} \;=\; (\quad \delta b_{gx} \quad \delta b_{gy} \quad \delta b_{gz} \quad \delta s_{gx} \quad \delta s_{gy} \quad \delta s_{gz} \quad)^T$$

where

$$\frac{\partial f_g}{\partial b_{gx}} = \frac{-2(\ell_{gx} - b_{gx})}{(1 + s_{gx})^2} \qquad \frac{\partial f_g}{\partial b_{gy}} = \frac{-2(\ell_{gy} - b_{gy})}{(1 + s_{gy})^2}$$

$$\frac{\partial f_g}{\partial b_{gz}} = \frac{-2(\ell_{gz} - b_{gz})}{(1 + s_{gz})^2} \qquad \frac{\partial f_g}{\partial s_{gx}} = \frac{-2(\ell_{gx} - b_{gx})^2}{(1 + s_{gx})^3}$$

$$\frac{\partial f_g}{\partial s_{gy}} = \frac{-2(\ell_{gy} - b_{gy})^2}{(1 + s_{gy})^3} \qquad \frac{\partial f_g}{\partial s_{gz}} = \frac{-2(\ell_{gz} - b_{gz})^2}{(1 + s_{gz})^3}$$

$$\frac{\partial f_g}{\partial \ell_{gx}} = \frac{2(\ell_{gx} - b_{gx})}{(1 + s_{gx})^2} \qquad \frac{\partial f_g}{\partial \ell_{gy}} = \frac{2(\ell_{gy} - b_{gy})}{(1 + s_{gy})^2}$$

$$\frac{\partial f_g}{\partial \ell_{gz}} = \frac{2(\ell_{gz} - b_{gz})}{(1 + s_{gz})^2}$$

For gyroscopes,

$$
A = \begin{pmatrix}
\cdots & \cdots & \cdots \\
\dfrac{\partial f_\omega}{\partial b_{\omega x}} & \dfrac{\partial f_\omega}{\partial b_{\omega y}} & \dfrac{\partial f_\omega}{\partial b_{\omega z}} \\
\cdots & \cdots & \cdots
\end{pmatrix}
$$

$$
B = \begin{pmatrix}
\cdots & \cdots & \cdots & 0 & 0 & 0 & 0 & 0 & 0 \\
0 & 0 & 0 & \dfrac{\partial f_\omega}{\partial \ell_{\omega x}} & \dfrac{\partial f_\omega}{\partial \ell_{\omega y}} & \dfrac{\partial f_\omega}{\partial \ell_{\omega z}} & 0 & 0 & 0 \\
0 & 0 & 0 & 0 & 0 & 0 & \cdots & \cdots & \cdots
\end{pmatrix}
$$

$$
\hat{\underline{\delta}} = \begin{pmatrix} \delta b_{\omega x} & \delta b_{\omega y} & \delta b_{\omega z} \end{pmatrix}^T
$$

$$
\underline{\ell} = \begin{pmatrix} \cdots & \cdots & \cdots & \ell_{\omega x} & \ell_{\omega y} & \ell_{\omega z} & \cdots & \cdots & \cdots \end{pmatrix}^T
$$

$$
\hat{\underline{r}} = \begin{pmatrix} \cdots & \cdots & \cdots & r_{\omega x} & r_{\omega y} & r_{\omega z} & \cdots & \cdots & \cdots \end{pmatrix}^T
$$

$$
\underline{w} = \begin{pmatrix} \cdots & f_\omega(\underline{x}, \underline{\ell}) & \cdots \end{pmatrix}^T
$$

where

$$
\frac{\partial f_\omega}{\partial b_{\omega x}} = -2(\ell_{\omega x} - b_{\omega x}) \qquad \frac{\partial f_\omega}{\partial b_{\omega y}} = -2(\ell_{\omega y} - b_{\omega y})
$$

$$
\frac{\partial f_\omega}{\partial b_{\omega z}} = -2(\ell_{\omega z} - b_{\omega z}) \qquad \frac{\partial f_\omega}{\partial \ell_{\omega x}} = 2(\ell_{\omega x} - b_{\omega x})
$$

$$
\frac{\partial f_\omega}{\partial \ell_{\omega y}} = 2(\ell_{\omega y} - b_{\omega y}) \qquad \frac{\partial f_\omega}{\partial \ell_{\omega z}} = 2(\ell_{\omega z} - b_{\omega z})
$$

The solution of this system of equations is given by

$$
\begin{aligned}
\hat{\underline{\delta}} &= -N^{-1}\underline{u} \\
&= -\left[A^T\left(BC_\ell B^T\right)^{-1}A + C_x^{-1}\right]^{-1}A^T\left(BC_\ell B^T\right)^{-1}\underline{w} \tag{4.29} \\
C_{\hat{x}} &= N^{-1} = \left[A^T\left(BC_\ell B^T\right)^{-1}A + C_x^{-1}\right]^{-1} \tag{4.30}
\end{aligned}
$$

where N is the coefficient matrix of the normal equations. Since the correlation among three axes are not known, it is assumed that the measurements are uncorrelated. So, C_ℓ and $(BC_\ell B^T)^{-1}$ will be diagonal. Then, the i-th diagonal element, corresponding to the i-th gravity measurement, can be expressed as

$$
\begin{aligned}
M_{ii}^{-1} &= \left(BC_\ell B^T\right)_{ii}^{-1} \\
&= \left[\sigma_{\ell gx}^2\left(\frac{\partial f_g}{\partial \ell_{gx}}\right)^2 + \sigma_{\ell gy}^2\left(\frac{\partial f_g}{\partial \ell_{gy}}\right)^2 + \sigma_{\ell gz}^2\left(\frac{\partial f_g}{\partial \ell_{gz}}\right)^2\right]_i^{-1} \tag{4.31}
\end{aligned}
$$

Hence, the normal matrix will be symmetric and the coefficient matrix of the normal equation can be composed directly without generating intermediate matrices, i.e. A and B, as follows:

$$
\begin{aligned}
N_{ij} &= \sum_k A_{ki} M_{kk}^{-1} A_{kj} + \left(C_x^{-1}\right)_{ij}, \quad i = 1, 2, \cdots, m \quad j = i, \cdots, m \tag{4.32} \\
u_i &= \sum_k A_{ki} M_{ii}^{-1} w_i, \quad i = 1, 2, \cdots, m \tag{4.33}
\end{aligned}
$$

where m is the number of parameters. Using these equations and the widely used numerical algorithm such as Cholesky's decomposition, we can significantly reduce the amount of memory required for storing the matrices.

4.1.4 Calibration Methodology

Although this method does not require the IMU axes to be aligned to the local-level frame, to avoid a singularity in the calculation of the inverse of the normal matrix for the bias, scale factor, and nonorthogonality model, at least nine different attitudes should be measured. Similarly, for the bias and scale factor model, six or more attitude measurements are needed. As shown in Figure 4.4, possible attitudes would be each face down, each side down and each corner down, which make for six, twelve, and eight different attitude measurements, respectively.
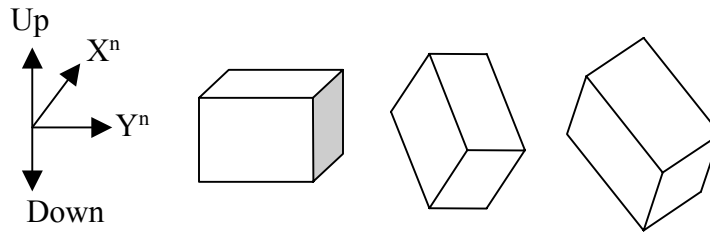
Figure 4.4: IMU measurement attitudes

For a triad of accelerometers, the attitudes of each face down should be enough for the determination of the bias and scale factor. Because the attitudes of each side down and each corner down correspond to the relationship between the two axes and three axes in an IMU, they contribute to the determination of the nonorthogonalities. For a triad of gyroscopes, the number of axes that have values significantly larger than zero can change according to

the latitude and the heading of an IMU. In mid-latitude areas, when one of the three axes points to east or west, the number can be two for the attitudes of each face down, one for those of each side down, and two for those of each corner down. Figure 4.5 shows an example of rotation schemes for eighteen different measurements, which can be implemented using two-degree-of-freedom rotational frames.

Figure 4.5: An example of IMU rotation scheme

In the case that the IMU is strapped down in a vehicle without using a rotational frame, if it is in mid-latitude area the calibration of gyroscopes can be accomplished with horizontal measurements only, as shown in Figure 4.6. If the vehicle is on a tilted surface or can be tilted, the method works for the areas near the equator or poles of the Earth as well.
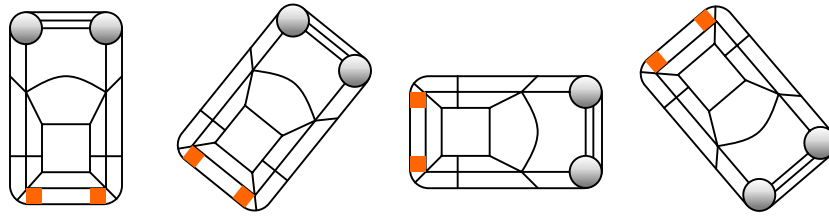
Figure 4.6: Calibration with horizontal measurements
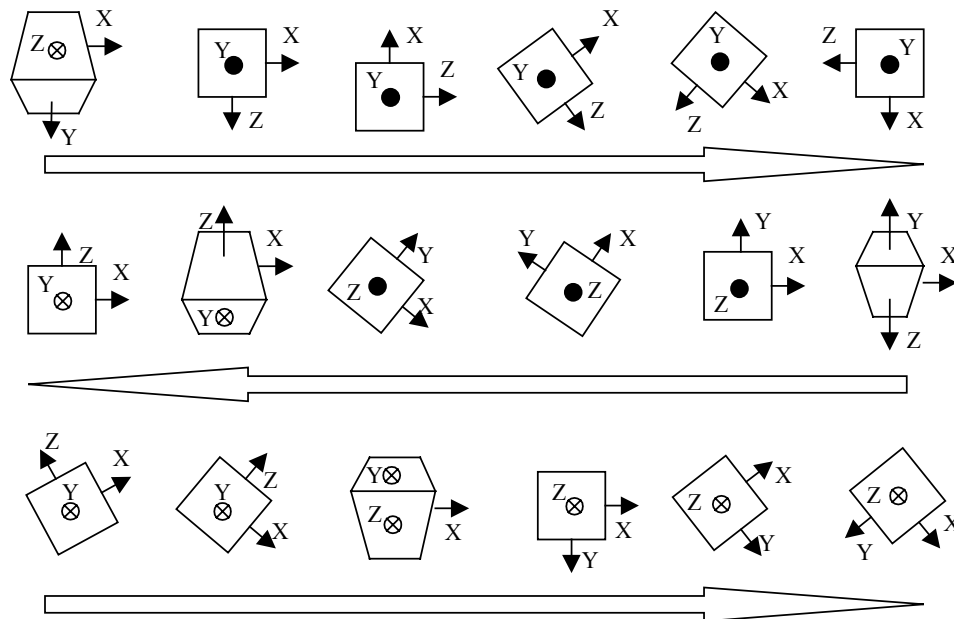
However, for accelerometer calibration, if the vehicle is on the level surface, the calculation would generate numerical problems. For the test of the accelerometer calibration, a dataset was simulated for 15° tilted area with the true parameter values given in Table 4.1. For gyroscope calibration, the dataset was generated for a level surface in the latitude 50°. Table 4.1 shows that the gyroscope calibration works well with only horizontal measurements. The accelerometer calibration works perfectly for x and y biases. Z-bias has an error about 30 $mGal$ and all scale factors are not so reliable. Least squares estimation splits the total error between two mutually unobservable states per initial uncertainty.

4.1.5   Sensitivity of the Method

The Earth's rotation rate does not change with the position. However, the normal gravity is not the same as the actual gravity, and the difference between them, i.e. the gravity anomaly, is dependent on position. So, it is necessary to analyze the sensitivity of the method to the reference gravity error. Table 4.2, obtained by applying the new calibration method to

Table 4.1: Calibration with horizontal measurements

		Accelerometer (tilt=15°)		Gyroscope (tilt=0°)
		Bias (mGal)	Scale factor (ppm)	Bias (deg/hr)
True	X	500.0000	0.0000	1.0000
	Y	600.0000	0.0000	2.0000
	Z	700.0000	0.0000	3.0000
Calib.	X	500.0004	-192.4012	0.9997
	Y	600.0005	-192.4012	1.9994
	Z	730.2500	45.7485	3.0022

an error-free dataset generated assuming that the reference gravity is 9.8 m/s^2, shows the estimation errors of the calibration parameters according to the given reference gravity errors. It can be seen that the errors are transferred not to the biases and nonorthogonalities but to the scale factors. Further, as shown in Figure 4.7, the scale factor errors are reciprocally proportional to the reference gravity errors.

Let's analyze the sensitivity of the simple calibration method that needs to align each accelerometer channel of the IMU to the direction of the gravity vector. When one channel is aligned to the gravity vector, the specific force measurement will be g and $-g$ for the up

Table 4.2: Sensitivity of the new calibration method to the reference gravity errors

Gravity (mGal)	-150	-100	-50	0	50	100	150
b_{gx} (mGal)	2.5E-09	7.2E-10	6.7E-11	-4.4E-11	-1.4E-10	-7.9E-10	-2.5E-09
b_{gy} (mGal)	-2.4E-09	-6.9E-10	-6.4E-11	-4.4E-11	1.3E-10	7.7E-10	2.5E-09
b_{gz} (mGal)	-2.1E-10	-5.9E-11	-1.6E-11	4.4E-11	4.4E-11	8.9E-11	2.5E-10
s_{gx} (ppm)	153	102	51	-5.5E-11	-51	-102	-153
s_{gy} (ppm)	153	102	51	-5.5E-11	-51	-102	-153
s_{gz} (ppm)	153	102	51	-5.5E-11	-51	-102	-153
θ_{gyz} (arc sec)	7.6E-09	2.3E-09	3.4E-10	1.3E-11	-3.0E-10	-2.3E-09	-7.6E-09
θ_{gzx} (arc sec)	-1.5E-09	-4.4E-10	-6.3E-11	-1.3E-11	5.4E-11	4.3E-10	1.4E-09
θ_{gzy} (arc sec)	-1.5E-09	-4.5E-10	-6.5E-11	-1.3E-11	5.6E-11	4.5E-10	1.5E-09

and down direction, respectively:

$$\ell_{up} = b + (1+s)g \qquad (4.34)$$

$$\ell_{down} = b - (1+s)g \qquad (4.35)$$

where b and s are the bias and scale factor of the channel and g is the magnitude of the
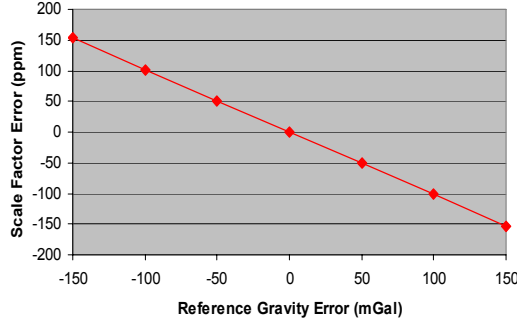
Figure 4.7: Scale Factor Error Sensitivity

gravity vector. The bias and scale factor are calculated as:

$$b = (\ell_{up} + \ell_{down})/2 \tag{4.36}$$

$$s = (\ell_{up} - \ell_{down} - 2g)/2g \tag{4.37}$$

Hence, the bias is not affected by the error in the reference gravity value. However, the reference gravity error does influence the scale factor calculation. To calculate the effect of the reference gravity error on the estimation of scale factor, we assume error-free measurements, $\ell_{up} - \ell_{down} = 2g$ and use $g + \delta g$ instead of g in Eq. (4.37). Then, the scale factor error from the reference gravity error will be

$$\delta s = \frac{-\delta g}{g + \delta g}. \tag{4.38}$$

If we use $g = 9.8 \ m/s^2$ and calculate δs for some values of δg, the scale factor sensitivity can be obtained as shown in Table 4.3.

Table 4.3: Scale factor sensitivity of the simplest calibration method

δg (mGal)	-150	-100	-50	0	50	100	150
δs (ppm)	153	102	51	0	-51	-102	-153

The comparison of Table 4.2 and 4.3 shows that both methods have the same sensitivity to the reference gravity error and therefore the new calibration method works physically in the same manner as the simplest method in the determination of the bias and scale factor.

4.2 Alignment

The alignment of an IMU is the determination of the DCM C_b^n, and is accomplished by two steps, leveling and gyrocompassing. Leveling refers to obtaining the roll and pitch using the accelerometer outputs and gyrocompassing refers to obtaining the heading information using the gyroscope outputs. For the IMUs whose bias and noise levels are smaller than the value of the Earth's rotation rate, such as navigation-grade and high-end tactical grade IMUs, the analytic coarse alignment method followed by the fine alignment can be applied to estimate the IMU's attitude information. The coarse alignment can be calculated using the averaged data for two or three minutes in stationary mode. So, the analytical coarse alignment yields averaged attitude. Since the instantaneous attitude of an IMU is continuously changing by

outer disturbances, the fine alignment technique is needed. The fine alignment is to estimate

the attitude of an IMU with higher accuracy in time, and in commercial aircrafts is used to

detect small attitude changes caused by wind gusts, loading of passengers and cargo, fuel

ingestion and so on (Britting, 1971, p. 209). For low-end tactical-grade, automotive-grade,

and consumer-grade IMUs, the external heading measurements using magnetic compasses

or velocity matching alignment technique are usually used.

4.2.1 Analytic Coarse Alignment

If $\underline{\nu}$ is defined as the vector orthogonal to the specific force vector, $\underline{f}$, and the angular rate

vector, $\underline{\omega}_{ib}$, at the same time, i.e. $\underline{\nu} = \underline{f} \times \underline{\omega}_{ib}$, we can have (Britting, 1971, p. 199)

$$
\begin{pmatrix}
\underline{f}^b \\
\underline{\omega}^b_{ib} \\
\underline{\nu}^b
\end{pmatrix}
= C^b_n
\begin{pmatrix}
\underline{f}^n \\
\underline{\omega}^n_{ib} \\
\underline{\nu}^n
\end{pmatrix}
\tag{4.39}
$$

Transposition of the upper equation yields

$$
\begin{pmatrix}
(\underline{f}^b)^T \\
(\underline{\omega}^b_{ib})^T \\
(\underline{\nu}^b)^T
\end{pmatrix}
=
\begin{pmatrix}
(\underline{f}^n)^T \\
(\underline{\omega}^n_{ib})^T \\
(\underline{\nu}^n)^T
\end{pmatrix}
C^n_b .
\tag{4.40}
$$

Then, the alignment matrix is obtained by

$$
C_b^n = \begin{pmatrix} (\underline{f}^n)^T \\ (\underline{\omega}_{ib}^n)^T \\ (\underline{\nu}^n)^T \end{pmatrix}^{-1} \begin{pmatrix} (\underline{f}^b)^T \\ (\underline{\omega}_{ib}^b)^T \\ (\underline{\nu}^b)^T \end{pmatrix} \tag{4.41}
$$

The solution of Eq. (4.41) exists except for the case that the IMU is at the Earth's poles, where the gravity vector is parallel to the Earth's rotation rate vector and therefore $\underline{\nu} = \underline{0}$. Since $\underline{f}^n = -\underline{g}^n = (\begin{array}{ccc} 0 & 0 & -\gamma \end{array})^T$ and $\underline{\omega}_{ib}^n = \underline{\omega}_{ie}^n = (\begin{array}{ccc} \omega_e \cos\varphi & 0 & -\omega_e \sin\varphi \end{array})^T$ in stationary mode,

$$
\begin{pmatrix} (\underline{f}^n)^T \\ (\underline{\omega}_{ib}^n)^T \\ (\underline{\nu}^n)^T \end{pmatrix}^{-1} = \begin{pmatrix} 0 & 0 & -\gamma \\ \omega_e \cos\varphi & 0 & -\omega_e \sin\varphi \\ 0 & -\gamma\omega_e \cos\varphi & 0 \end{pmatrix}^{-1}
$$

$$
= \begin{pmatrix} \dfrac{-\tan\varphi}{\gamma} & \dfrac{1}{\omega_e \cos\varphi} & 0 \\ 0 & 0 & \dfrac{-1}{\gamma\omega_e \cos\varphi} \\ \dfrac{-1}{\gamma} & 0 & 0 \end{pmatrix} \tag{4.42}
$$

The DCM C_b^n calculated by Eq. (4.41) usually does not satisfy the orthogonality and normality condition. This problem can be resolved if we transform the DCM into the Euler angles using Eq. (2.5) $\sim$ (2.7), and then transform the Euler angles again into the DCM using Eq. (2.4).

To investigate the errors of this method, perturbing Eq. (4.41) with

$$\tilde{\underline{f}}^b = -\underline{g}^b + \delta \underline{f}^b \tag{4.43}$$

$$\tilde{\underline{\omega}}^b_{ib} = \underline{\omega}^b_{ie} + \delta \underline{\omega}^b \tag{4.44}$$

$$\tilde{\underline{\nu}}^b = \underline{\nu}^b + \delta \underline{\nu}^b \tag{4.45}$$

results in

$$- E^n C_b^n = \begin{pmatrix} -\dfrac{\tan \varphi}{\gamma} & \dfrac{1}{\omega_e \cos \varphi} & 0 \\[2mm] 0 & 0 & \dfrac{-1}{\gamma \omega_e \cos \varphi} \\[2mm] \dfrac{-1}{\gamma} & 0 & 0 \end{pmatrix} \begin{pmatrix} (\delta \underline{f}^b)^T \\[2mm] (\delta \underline{\omega}^b)^T \\[2mm] (\delta \underline{\nu}^b)^T \end{pmatrix} \tag{4.46}$$

where ˜ denotes measurements. To simplify the situation, assume that the IMU is aligned to the navigation frame, i.e. $C_b^n = I$. Then, $\delta \underline{\nu}^b$ can be written to the first order as

$$\delta \underline{\nu}^b = \begin{pmatrix} \delta \nu_x & \delta \nu_y & \delta \nu_z \end{pmatrix}^T$$

$$= \delta \underline{f}^b \times \underline{\omega}^n_{ie} - \underline{g}^n \times \delta \underline{\omega}^b$$

$$= \begin{pmatrix} -\delta f_y \omega_e \sin \varphi + \gamma \delta \omega_y \\[2mm] \delta f_x \omega_e \sin \varphi + \delta f_z \omega_e \cos \varphi - \gamma \delta \omega_x \\[2mm] \delta f_y \omega_e \cos \varphi \end{pmatrix} \tag{4.47}$$

Using the above equation and setting $C_b^n = I$, Eq. (4.46) can be rewritten as

$$
\begin{pmatrix}
0 & \epsilon_D & -\epsilon_E \\
-\epsilon_D & 0 & \epsilon_N \\
\epsilon_E & -\epsilon_N & 0
\end{pmatrix}
=
\begin{pmatrix}
-\dfrac{\tan\varphi}{\gamma} & \dfrac{1}{\omega_e \cos\varphi} & 0 \\
0 & 0 & \dfrac{-1}{\gamma\omega_e \cos\varphi} \\
\dfrac{-1}{\gamma} & 0 & 0
\end{pmatrix}
\begin{pmatrix}
\delta f_x & \delta f_y & \delta f_z \\
\delta\omega_x & \delta\omega_y & \delta\omega_z \\
\delta\nu_x & \delta\nu_y & \delta\nu_z
\end{pmatrix}
$$

$$
=
\left(
\begin{array}{c|c|c}
\begin{aligned}
&-\dfrac{\delta f_x \tan\varphi}{\gamma}\\
&+\dfrac{\delta\omega_x}{\omega_e \cos\varphi}
\end{aligned}
&
\begin{aligned}
&-\dfrac{\delta f_y \tan\varphi}{\gamma}\\
&+\dfrac{\delta\omega_y}{\omega_e \cos\varphi}
\end{aligned}
&
\begin{aligned}
&-\dfrac{\delta f_z \tan\varphi}{\gamma}\\
&+\dfrac{\delta\omega_z}{\omega_e \cos\varphi}
\end{aligned}
\\ \hline
-\dfrac{\delta\nu_x}{\gamma\omega_e \cos\varphi}
&
-\dfrac{\delta\nu_y}{\gamma\omega_e \cos\varphi}
&
-\dfrac{\delta\nu_z}{\gamma\omega_e \cos\varphi}
\\ \hline
-\dfrac{\delta f_x}{\gamma}
&
-\dfrac{\delta f_y}{\gamma}
&
-\dfrac{\delta f_z}{\gamma}
\end{array}
\right)
\tag{4.48}
$$

Since each of ϵ_N, ϵ_E, ϵ_D appears twice in the left hand side of the above equation, averaging them using Eq. (4.47) yields

$$
\epsilon_N = \frac{\delta f_y}{\gamma}, \tag{4.49}
$$

$$
\epsilon_E = \frac{1}{2}\left(-\frac{\delta f_x}{\gamma} + \frac{\delta f_z}{\gamma}\tan\varphi - \frac{\delta\omega_z}{\omega_e}\sec\varphi\right), \tag{4.50}
$$

$$
\epsilon_D = -\frac{\delta f_y}{\gamma}\tan\varphi + \frac{\delta\omega_y}{\omega_e}\sec\varphi. \tag{4.51}
$$

Figure 4.8 shows the value of the second term on the right hand side of Eq. (4.51) for some gyroscope bias values at latitude 50°. The heading error would be about $6 \sim 30°$, if the gyroscope bias was $1 \sim 5°/hr$. If the bias is not estimated correctly in the fine alignment Kalman filter, the heading error would still remain even after filtering.
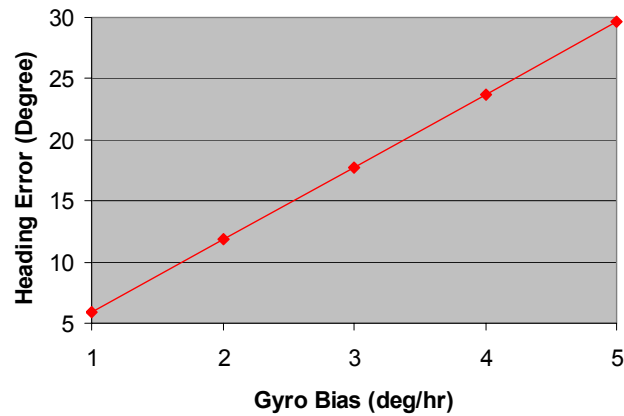
Figure 4.8: Coarse Alignment Error

4.2.2 Fine Alignment

The fine alignment phase uses the established DCM from either the coarse alignment technique or initialization data from stored heading or best available true heading (Rogers, 2000, p. 208). The initial estimate for the C_b^n is then refined using a Kalman filter. Although low-pass filter approach, which is simple and requires low number of computations, can also be applied, the Kalman filter approach has advantages in that both the accelerometer-based leveling and gyro-based heading alignment can occur simultaneously and in that the approach correctly accounts for all measurement errors (Farrell and Barth, 1998, p. 231).

The east channel gyro measurements are used for the heading refinement. Two types of measurements can be considered for the leveling, i.e. the north and east channel specific force measurements or the north and east channel velocity measurements. The former approach

can be found in Farrell and Barth (1998), and the latter in Rogers (2000), and both methods

are depicted in figures 4.10 and 4.9. While the former directly uses the specific force error

measurements in the Kalman filter, the latter integrates them once to obtain velocity errors.
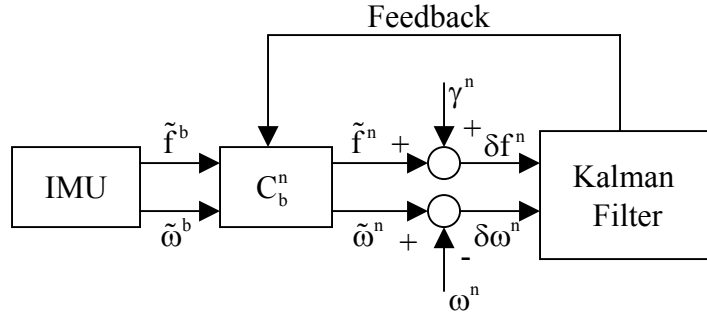

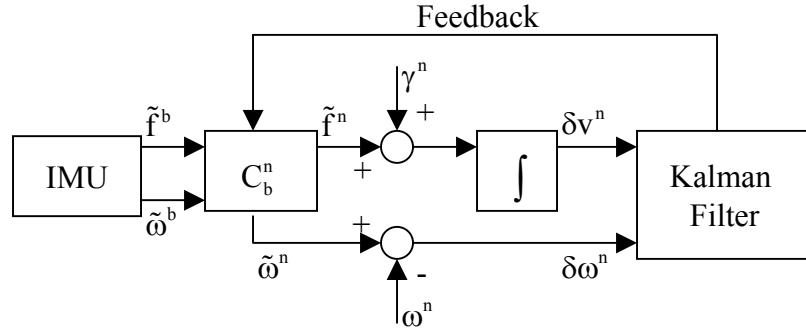Figure 4.9: Fine alignment with the specific force measurements

Figure 4.10: Fine alignment with the velocity measurements

The navigation frame specific force error measurement is described by

$$
\begin{aligned}
\delta \underline{f}^n &= \hat{C}_b^n \tilde{\underline{f}}^b - \underline{f}^n \\
&= (I - E^n)C_b^n(\underline{f}^b + \delta \underline{f}^b) - \underline{f}^n
\end{aligned}
$$

$$\approx \ C_b^n \underline{f}^b - E^n C_b^n \underline{f}^b + C_b^n \delta \underline{f}^b - \underline{f}^n$$

$$= \ -E^n C_b^n \underline{f}^b + C_b^n \delta \underline{f}^b$$

$$= \ (\underline{f}^n \times) \underline{\epsilon}^n + C_b^n \delta \underline{f}^b, \tag{4.52}$$

and similarly for the gyro measurement

$$\delta \underline{\omega}^n = \ \hat{C}_b^n \tilde{\underline{\omega}}^b - \underline{\omega}^n$$

$$= \ (I - E^n) C_b^n (\underline{\omega}^b + \delta \underline{\omega}^b) - \underline{\omega}^n$$

$$\approx \ C_b^n \underline{\omega}^b - E^n C_b^n \underline{\omega}^b + C_b^n \delta \underline{\omega}^b - \underline{\omega}^n$$

$$= \ -E^n C_b^n \underline{\omega}^b + C_b^n \delta \underline{\omega}^b$$

$$= \ (\underline{\omega}^n \times) \underline{\epsilon}^n + C_b^n \delta \underline{\omega}^b. \tag{4.53}$$

Since $\underline{f}^n = (\begin{matrix} 0 & 0 & -\gamma \end{matrix})^T$ and $\underline{\omega}^n = (\begin{matrix} \omega_e \cos \varphi & 0 & -\omega_e \sin \varphi \end{matrix})^T$ during the alignment, the measurement matrices for the first approach can be constructed from the first and second rows of Eq. (4.52) and from the second row of Eq. (4.53) as

$$\underline{z}_k = \begin{pmatrix} \delta f_N \\ \delta f_E \\ \delta \omega_E \end{pmatrix}, H_k = \begin{pmatrix} & & 0 & \gamma & 0 \\ 0_{3\times3} & 0_{3\times3} & -\gamma & 0 & 0 \\ & & -\omega_e \sin \varphi & 0 & -\omega_e \cos \varphi \end{pmatrix} \tag{4.54}$$

For the second approach the measurement matrices are described by

$$
\underline{z}_k = \begin{pmatrix} \delta v_N \\ \delta v_E \\ \delta \omega_E \end{pmatrix}, H_k = \begin{pmatrix} 0_{3\times 3} & \begin{array}{ccc} 1 & 0 & 0 \\ 0 & 1 & 0 \\ 0 & 0 & 0 \end{array} & \begin{array}{ccc} 0 & 0 & 0 \\ 0 & 0 & 0 \\ -\omega_e \sin\varphi & 0 & -\omega_e \cos\varphi \end{array} \end{pmatrix}.
\tag{4.55}
$$

4.2.3   Velocity Matching Alignment

When the IMU's performance is so poor that the bias and noise level are much greater than the Earth's rotation rate, the roll and pitch can be obtained with stationary accelerometer measurements, however, the heading can not be determined. Although magnetic sensors can be used to get the initial heading information, the errors of the sensors are hard to model. In this case the velocity information from the GPS can be used to align the IMU while in motion.

The position and velocity of the IMU can be initialized by copying those of the GPS after applying the lever-arm correction. On a level surface the roll and pitch are almost zeros, and the approximate heading can be calculated using the navigation frame velocity:
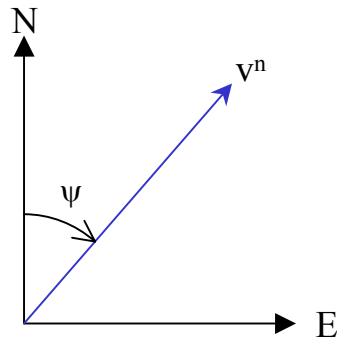
$$
\psi = \tan^{-1}(v_E/v_N)
\tag{4.56}
$$

Figure 4.11: Initial Heading

Therefore, the attitude of the IMU can be initialized by substituting these Euler angles into Eq.(2.4). Then, the attitude is refined with a Kalman filter by the velocity measurements as shown in Figure 4.12. The position of the IMU is reset with that of GPS every time GPS measurement comes.
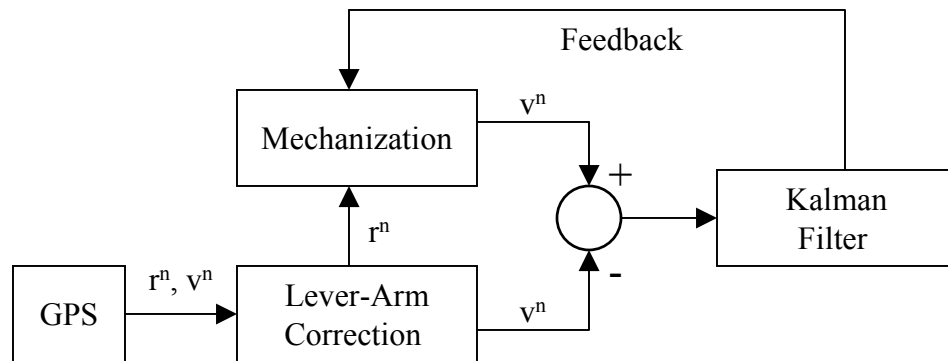

Figure 4.12: Velocity Matching Alignment

Assuming that the position is accurately known during the initialization process, the error

dynamics of the reduced-state model incorporating north and east velocity errors and attitude errors can be obtained by removing the columns and rows related to the position and down-velocity in Eq. (3.31) (Farrell and Barth, 1998, p.233):

$$
\dot{\underline{x}} = \begin{pmatrix} F_{11} & F_{12} \\ F_{21} & F_{22} \end{pmatrix} \underline{x} + G\underline{u}, \tag{4.57}
$$

where

$$
\underline{x} = \begin{pmatrix} \delta v_N & \delta v_D & \epsilon_N & \epsilon_E & \epsilon_D \end{pmatrix}^T,
$$

$$
F_{11} = \begin{pmatrix} \dfrac{v_D}{M+h} & -2\dfrac{v_E \tan\varphi}{N+h} \\[2mm] 2\omega_e \sin\varphi & \\ +\dfrac{v_E \tan\varphi}{N+h} & \dfrac{v_D + v_N \tan\varphi}{N+h} \end{pmatrix}, F_{12} = \begin{pmatrix} 0 & -f_D & f_E \\ f_D & 0 & -f_N \end{pmatrix},
$$

$$
F_{21} = \begin{pmatrix} 0 & \dfrac{1}{N+h} \\[2mm] \dfrac{-1}{M+h} & 0 \\[2mm] 0 & \dfrac{-\tan\varphi}{N+h} \end{pmatrix},
$$

$$F_{22} = \begin{pmatrix} 0 & \begin{array}{c} -\omega_e \sin\varphi \\ -\dfrac{v_E \tan\varphi}{N+h} \end{array} & \dfrac{v_N}{M+h} \\ \begin{array}{c} \omega_e \sin\varphi \\ +\dfrac{v_E \tan\varphi}{N+h} \end{array} & 0 & \begin{array}{c} \omega_e \cos\varphi \\ +\dfrac{v_E}{N+h} \end{array} \\ \dfrac{-v_N}{M+h} & \begin{array}{c} -\omega_e \cos\varphi \\ -\dfrac{v_E}{N+h} \end{array} & 0 \end{pmatrix},$$

$$G = \left(\begin{array}{ccc|ccc} c_{11} & c_{12} & c_{13} & 0 & 0 & 0 \\ c_{21} & c_{22} & c_{23} & 0 & 0 & 0 \\ \hline & 0_{3\times3} & & & -C_b^n & \end{array} \right), \underline{u} = \begin{pmatrix} \delta\underline{f}^b \\ \delta\underline{\omega}_{ib}^b \end{pmatrix}$$

and c_{ij}'s, $1 \le i,j \le 3$, are (i,j)-th elements of the DCM C_b^n. The measurement matrices are

$$\underline{z}_k = \begin{pmatrix} \delta v_N \\ \delta v_E \end{pmatrix}, H_k = \begin{pmatrix} 1 & 0 & 0 & 0 & 0 \\ 0 & 1 & 0 & 0 & 0 \end{pmatrix}. \tag{4.58}$$

After the velocity matching alignment is finished, the filter is switched to the nine-state or fifteen-state navigation Kalman filter.

4.3 Using Non-Holonomic Constraints

Non-holonomic constraints refer to the fact that unless the vehicle jumps off the ground or slides on the ground, the velocity of the vehicle in the plane perpendicular to the forward direction (x-axis) is almost zero (Sukkarieh, 2000). So, two non-holonomic constraints can

be considered as measurement updates to the navigation Kalman filter

$$v_y^b \approx 0 \tag{4.59}$$

$$v_z^b \approx 0. \tag{4.60}$$

The computed velocity in the body frame can be expressed as:

$$\hat{\underline{v}}^b = \hat{C}_n^b \hat{\underline{v}}^n = \left(\hat{C}_b^n \right)^T \hat{\underline{v}}^n. \tag{4.61}$$

Perturbing the upper equation gives

$$
\begin{aligned}
\underline{v}^b + \delta \underline{v}^b &= [(I - E^n) C_b^n]^T (\underline{v}^n + \delta \underline{v}^n) \\
&= C_n^b (I + E^n)(\underline{v}^n + \delta \underline{v}^n).
\end{aligned}
\tag{4.62}
$$

Collecting terms to the first order ,

$$
\begin{aligned}
\delta \underline{v}^b &= C_n^b \delta \underline{v}^n + C_n^b E^n \underline{v}^n \\
&= C_n^b \delta \underline{v}^n - C_n^b (\underline{v}^n \times) \underline{\epsilon}^n.
\end{aligned}
\tag{4.63}
$$

From the second and third rows, the measurement equations can be constructed as:

$$\underline{z}_k = \left(\begin{array}{cc} \delta v_y^b & \delta v_z^b \end{array} \right)^T, \tag{4.64}$$

$$
H_k = \left(\begin{array}{ccc|ccc|ccc}
0 & 0 & 0 & C_{12} & C_{22} & C_{32} & \begin{array}{c} -v_D C_{22} \\ +v_E C_{32} \end{array} & \begin{array}{c} v_D C_{12} \\ -v_N C_{32} \end{array} & \begin{array}{c} -v_E C_{12} \\ +v_N C_{22} \end{array} \\
\hline
0 & 0 & 0 & C_{13} & C_{23} & C_{33} & \begin{array}{c} -v_D C_{23} \\ +v_E C_{33} \end{array} & \begin{array}{c} v_D C_{13} \\ -v_N C_{33} \end{array} & \begin{array}{c} -v_E C_{13} \\ +v_N C_{23} \end{array}
\end{array} \right), \tag{4.65}
$$

where C_{ij}'s, $1 \leq i, j \leq 3$, are the (i, j)-th elements of the DCM C_b^n.

As shown in Figure 4.13, the velocity output of the INS mechanization, $\underline{v}^n$, is pre-multiplied by C_n^b to yield the body frame velocity, $\underline{v}^b$. The second and third elements of $\underline{v}^b$ themselves are used as the measurements in the Kalman filter. The estimated errors are fed back to the mechanization.
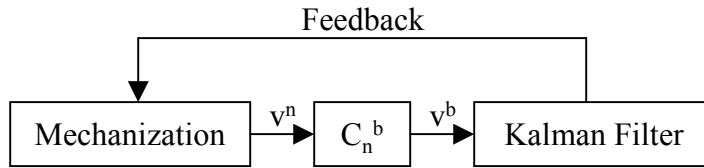

Figure 4.13: Implementation of the non-holonomic constraints

4.4 Limiting Attitude Error Growth

When the vehicle's velocity is zero, for the navigation-grade or high-end tactical-grade IMUs, the fine alignment can be applied to correct the attitude errors if the GPS position is available. However, for the low-end tactical-grade, automotive-grade, and consumer-grade IMUs, the heading is susceptible to meandering because the gyrocompassing cannot be applied.

Since it is hard to model magnetic sensor errors, the heading error equations for general external heading measurements shall be derived in the sequel. From Eq. (2.7) and (3.3), the heading can be expressed as

$$
\begin{aligned}
\hat{\psi} &= \tan^{-1}\left(\frac{\hat{c}_{21}}{\hat{c}_{11}}\right) \\
&= \tan^{-1}\left(\frac{c_{11}\epsilon_D + c_{21} - c_{31}\epsilon_N}{c_{11} - c_{21}\epsilon_D + c_{31}\epsilon_E}\right),
\end{aligned}
\tag{4.66}
$$

where C_{ij}'s, $1 \le i, j \le 3$, are the (i,j)-th elements of the DCM C_b^n. Hence, the error equation can be expressed as

$$
\delta\psi = \frac{\partial\hat{\psi}}{\partial\epsilon_N}\epsilon_N + \frac{\partial\hat{\psi}}{\partial\epsilon_E}\epsilon_E + \frac{\partial\hat{\psi}}{\partial\epsilon_D}\epsilon_D,
\tag{4.67}
$$

where

$$
\begin{aligned}
\frac{\partial\hat{\psi}}{\partial\epsilon_N} &= \frac{-c_{31}\hat{c}_{11}}{\hat{c}_{11}^2 + \hat{c}_{21}^2} \approx \frac{-\hat{c}_{31}\hat{c}_{11}}{\hat{c}_{11}^2 + \hat{c}_{21}^2}, \\
\frac{\partial\hat{\psi}}{\partial\epsilon_E} &= \frac{-c_{31}\hat{c}_{21}}{\hat{c}_{11}^2 + \hat{c}_{21}^2} \approx \frac{-\hat{c}_{31}\hat{c}_{21}}{\hat{c}_{11}^2 + \hat{c}_{21}^2}, \\
\frac{\partial\hat{\psi}}{\partial\epsilon_D} &= \frac{c_{11}\hat{c}_{11} + c_{21}\hat{c}_{21}}{\hat{c}_{11}^2 + \hat{c}_{21}^2} \approx 1.
\end{aligned}
$$

The heading measurement together with the zero velocity measurements would give the following measurement matrices:

$$
\underline{z}_k = \begin{pmatrix} \delta v_N \\ \delta v_E \\ \delta \psi \end{pmatrix}, H_k = \left(\begin{array}{c|ccc|ccc} & 1 & 0 & 0 & 0 & 0 & 0 \\ 0_{3\times3} & 0 & 1 & 0 & 0 & 0 & 0 \\ & 0 & 0 & 0 & \dfrac{\partial \hat{\psi}}{\partial \epsilon_N} & \dfrac{\partial \hat{\psi}}{\partial \epsilon_E} & \dfrac{\partial \hat{\psi}}{\partial \epsilon_D} \end{array} \right)
\tag{4.68}
$$

In the case where there is no external heading measurement, instead of proceeding with the INS mechanization, we can take the DCM at the time right before the vehicle's velocity becomes zero and only perform the leveling using the specific force measurements. This will prevent the heading from meandering. The measurement matrices in this case will be

$$
\underline{z}_k = \begin{pmatrix} \delta f_N \\ \delta f_E \end{pmatrix}, H_k = \left(\begin{array}{ccc|ccc|ccc} 0 & 0 & 0 & 0 & 0 & 0 & 0 & \gamma & 0 \\ 0 & 0 & 0 & 0 & 0 & 0 & -\gamma & 0 & 0 \end{array} \right).
\tag{4.69}
$$

Chapter 5

Tests and Results

This chapter describes the tests and analysis for the methods proposed in the previous chapters. Two tests were conducted using the NovAtel BDS$^{\text{TM}}$ system on September 2 and November 11, 2001. The tests took place at one of the University of Calgary's parking lots. The GPS master station was set up on the roof of the Geomatics Engineering building where a number of very precise control pillars can be used.

5.1 System Configuration

The NovAtel Black Diamond System (BDS$^{\text{TM}}$) and other commercial software were used in the thesis. As shown in Figure 5.1, the BDS$^{\text{TM}}$ system is a tightly integrated GPS/INS

83

system consisting of (NovAtel, Inc., 2001):

- **BDS$^{\text{TM}}$ Controller**: the controller is a high performance, high accuracy, NovAtel OEM4 GPS receiver with a PC card slot for raw GPS/INS data logging. All data including GPS, IMU, and External trigger, are passed through the controller. So the controller time-tags all non-GPS data with the GPS time,

- **BDS$^{\text{TM}}$ Sensor**: BDS$^{\text{TM}}$ uses a Honeywell HG1700 IMU containing a triad of accelerometers and a triad of miniature, low cost tactical-grade ring laser gyroscopes, see Table 5.1 for the specification of the HG1700 unit,

- **BDS$^{\text{TM}}$ Software**: a post processing software which processes the master GPS and rover GPS/INS files.

The antenna (NovAtel GPS-600) and the IMU were mounted on top of a passenger vehicle using a rack mount as shown in Figure 5.2. The whole system was powered by 12V output through the cigarette jack of the vehicle. After the initialization process of the system, the controller logs the raw GPS and IMU measurements into a compact flash memory card through the PC card adapter.

To check the performance of the newly developed navigation frame INS mechanization and the results of velocity matching alignment software, the University of Calgary's GPS/INS integration software package the KINGSPAD$^{\text{TM}}$ (KINematic Geodetic System for Posi-

Figure 5.1: The BDS$^{\text{TM}}$ system, Courtesy of NovAtel Inc., Canada

Figure 5.2: Instrument setup

Table 5.1: The specification of HG1700 IMU (Honeywell, Inc.)

Specification	Value
Gyro Input Range	$\pm 1,000$ deg/sec
Gyro Rate Scale Factor	100 ppm
Gyro Rate Bias	1.0 deg/hr to 10 deg/hr
Angular Random Walk	0.125 deg/$\sqrt{}$hr to 0.3 deg/$\sqrt{}$hr
Accelerometer Range	± 50 g
Accelerometer Linearity	500 ppm
Accelerometer Scale Factor	300 ppm
Accelerometer Bias	1.0 mg (980 mGal)

tions and Attitude Determination) software was used (Schwarz and El-Sheimy, 2000). The

KINGSPAD$^{\text{TM}}$ software implements a de-centralized Kalman filter which runs two Kalman

filters in parallel, the INS filter being the master and the GPS filter being the local. The

INS master filter includes 15 states, 3 for position, 3 for velocity, 3 for misalignment, 3 for

gyro drifts, and 3 for accelerometer biases. The GPS filter includes 6 basic states – 3 states

for position ($\underline{r}^e$) and 3 states for velocity ($\underline{v}^e$) – and $n-1$ states for bias terms related to

the double difference phase ambiguities ($\nabla\Delta N$), where n is the number of satellites used

in the computation. The Waypoint GrafNav software was also used as a second reference

especially for generating the reference GPS trajectory.

5.2 Test Dataset

The data collection started, for both datasets, after about a 30 minutes warming-up period for the system. Each test dataset is composed of three parts as shown in Figure 5.3, the field calibration, stationary alignment, and motion tests to assess the velocity matching alignment and the non-holonomic constraints.
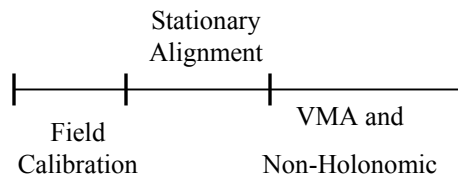

Figure 5.3: Test dataset

For the field calibration part, only up/down measurements were made for the first test and additional two tilt measurements were made for the second test. The measurement time for each attitude was about 2 minutes for the first test and 3 minutes for the second test. The stationary alignment period lasted for about fifteen minutes in which analytic coarse alignment and fine alignment techniques were applied. Then, for the first test, the vehicle was driven for about 20 minutes at the speed of about 30 km/hr with frequent turns to collect data for the testing of the velocity matching alignment and the non-holonomic constraints. For the second test, the vehicle was accelerated such that the speed could vary from 20 to

70 km/hr and the test time, for the testing of the velocity matching alignment and the non-holonomic constraints, lasted about 30 minutes.

5.3 Data Processing

The BDS$^{\text{TM}}$ controller stores GPS and IMU data in one file. Two conversion modules (SCALE_HG and NOV2KPD) were developed as shown in Figure 5.4 to extract the IMU data. SCALE_HG module scales the raw IMU measurements into *double* format and NOV2KPD module extracts the raw IMU measurements and stores them in their native format, i.e. *long int* format except for the time data (*double*). The graphic user interface and data reading
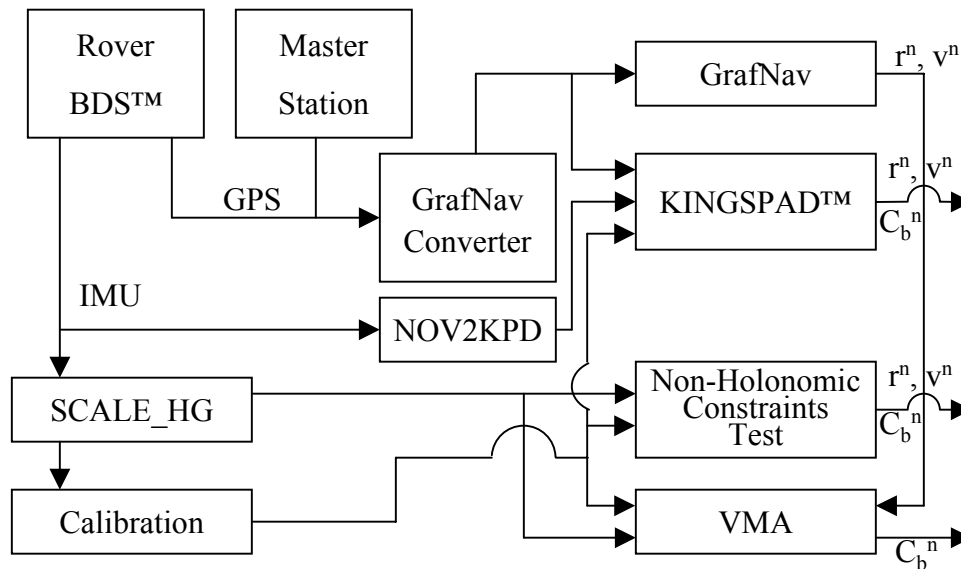

Figure 5.4: Data processing

modules of the KINGSPAD^{TM} software were modified to accept the HG1700 IMU data. The scaled file was used in the calibration, velocity matching alignment, and non-holonomic constraints test modules. The calibration results were passed to the KINGSPAD^{TM} software and other modules. The velocity matching alignment and non-holonomic constraints test modules use the navigation frame INS mechanization developed by the author.

The master station and rover GPS files are converted into GPB format (the GPS binary format used in the Waypoint and KINGSPAD^{TM} software) using the conversion module in the Waypoint software (Waypoint Consulting, Inc., 2000) so that they can be used in the KINGSPAD^{TM} and the GrafNav software. GPS data was collected at 1 Hz and processed to get the position and velocity in the navigation frame using the GrafNav software and the trajectories of the first and second datasets are shown in Figure 5.5. The GPS velocities from the GrafNav software were used in the velocity matching alignment and position information was used as a reference for all comparisons.
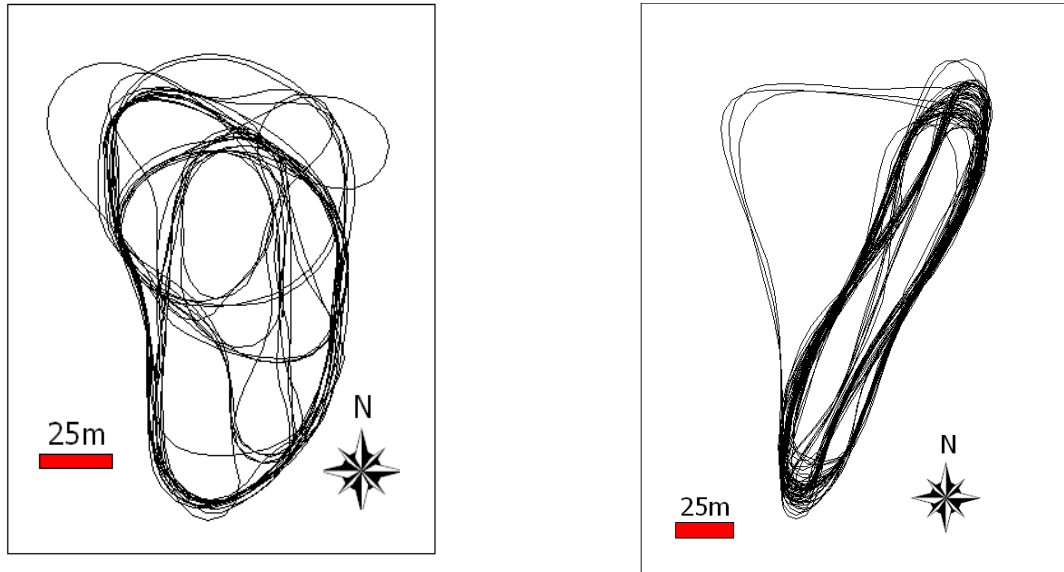
(a) The first dataset

(b) The second dataset

Figure 5.5: The reference GPS trajectories

5.4 Field Calibration Method

The first dataset included six different attitude measurements to calibrate the IMU. The measurement time lasted for about two minutes for each attitude. For the second dataset, however, the measurement time was extended to three minutes and eight different attitude measurements were made including additional two tilt measurements. The standard deviations of the measurements for both datasets are listed in Tables 5.2 and 5.3.

Table 5.2: Statistics of the first calibration observations

		Accel (m/s^2)			Gyro (deg/hr)		
		X	Y	Z	X	Y	Z
X-Up	Mean	9.79329	0.43312	-0.27051	11.12	-0.43	10.62
	STD	0.00111	0.00097	0.00090	2.07	3.28	5.55
X-Down	Mean	-9.80901	-0.04618	-0.13010	-13.25	5.75	5.11
	STD	0.00102	0.00090	0.00087	2.46	13.12	7.55
Y-Up	Mean	0.13775	9.77903	-0.80093	-5.51	12.26	5.51
	STD	0.00121	0.00103	0.00097	2.15	1.97	5.84
Y-Down	Mean	0.26497	-9.80174	0.12796	10.92	-9.95	9.85
	STD	0.00113	0.00098	0.00092	3.44	1.92	5.75
Z-Up	Mean	0.15963	-0.21825	9.81073	9.50	-0.11	11.81
	STD	0.00072	0.00062	0.00057	1.28	1.86	3.42
Z-Down	Mean	-0.01031	-0.21687	-9.80065	3.94	-33.80	-8.33
	STD	0.00125	0.00104	0.00099	5.49	17.06	5.99

Table 5.3: Statistics of the second calibration observations

		Accel (m/s^2)			Gyro (deg/hr)		
		X	Y	Z	X	Y	Z
X-Up	Mean	9.79590	0.04935	-0.39474	12.19	15.86	0.15
	STD	0.00062	0.00058	0.00058	1.75	1.57	4.39
X-Down	Mean	-9.79650	-0.03323	-0.58406	-11.78	-9.11	-0.35
	STD	0.00064	0.00059	0.00060	1.71	1.25	4.52
Y-Up	Mean	0.04615	9.78761	-0.55393	-10.63	11.37	-3.06
	STD	0.00054	0.00051	0.00051	1.45	1.08	3.92
Y-Down	Mean	0.19833	-9.80909	-0.13671	7.75	-11.90	1.15
	STD	0.00083	0.00076	0.00077	2.54	1.76	5.85
Z-Up	Mean	0.29056	-0.03159	9.81156	2.44	7.89	12.53
	STD	0.00065	0.00059	0.00060	1.84	1.22	4.52
Z-Down	Mean	0.27111	0.28437	-9.79355	1.94	-8.27	-11.51
	STD	0.00063	0.00057	0.00058	2.25	1.54	4.42
Tilt 1	Mean	6.04270	-0.31311	7.72498	14.64	-0.62	3.54
	STD	0.00063	0.00060	0.00059	1.71	1.34	4.48
Tilt 2	Mean	-0.28006	-5.84316	7.88373	-1.15	-14.76	3.96
	STD	0.00063	0.00058	0.00059	1.67	1.24	4.51

The standard deviations of the first dataset are larger than those of the second dataset. Especially, when the IMU's attitude was x-down or z-down, the standard deviations of the y-gyroscopes measurements are much higher than the others, over 10 deg/hr. For the second dataset, although the standard deviations of other gyroscope channels are reduced, the z-gyroscope's standard deviations are still high. However, they are more regularly distributed than those of the first dataset.

The accelerometer calibration was done using the bias and scale factor model, Eq. (4.27). Table 5.4 lists the calibration results of the first and second datasets. Since the calibration of the first dataset was performed with only six different attitude measurements, all standard deviations of the calibrated parameters are, as expected, higher than those estimated in the calibration of the second dataset. The calibration results for the second dataset are much different than the first one; especially, the y-accelerometer bias changed by about 780 $mGal$ and y-gyroscope bias also changed by about 4.6 deg/hr. However, the biases and scale factors of the accelerometers are smaller than those specified by the manufacturer, and the gyroscope biases are in the order of $\pm 1 \sim 2.5$ deg/hr level.

To check the effect of the calibration results on the positioning performance of the INS mechanization, the calibration results were used in the initial configuration file of the KINGSPAD$^{\text{TM}}$ software. The software was executed in three different initial conditions in free inertial navigation mode – the first run without using any calibration results, the second run with the

Table 5.4: Calibration results

		Accelerometer				Gyroscope	
		Bias (mGal)		Scale factor (ppm)		Bias (deg/hr)	
		Value	STD	Value	STD	Value	STD
Sep. 02	X	-174	4.3	5	4.5	-1.37	0.50
	Y	356	4.1	143	4.1	-2.44	0.32
	Z	571	3.3	58	3.4	2.30	0.68
Nov. 11	X	-487	2.4	118	2.6	0.69	0.07
	Y	-417	2.4	-30	2.5	1.44	0.06
	Z	734	2.0	72	2.2	0.15	0.17

accelerometer calibration results only, and the third run with both gyroscope and accelerometer calibration results. Figure 5.6 shows the processing results for the first dataset.

The reference trajectories for this and all other figures in the thesis, were obtained using the double-differenced GPS measurements. Their accuracy is, therefore, good to centimetre to decimetre level. As shown in the figure, without using any calibration information, the horizontal positioning error is about 5 km in 20 minutes. When the accelerometer calibration results were used, the error is reduced to 3 km in 20 minutes. Therefore, these results clearly indicate that the accelerometer calibration with only six different attitude measurements
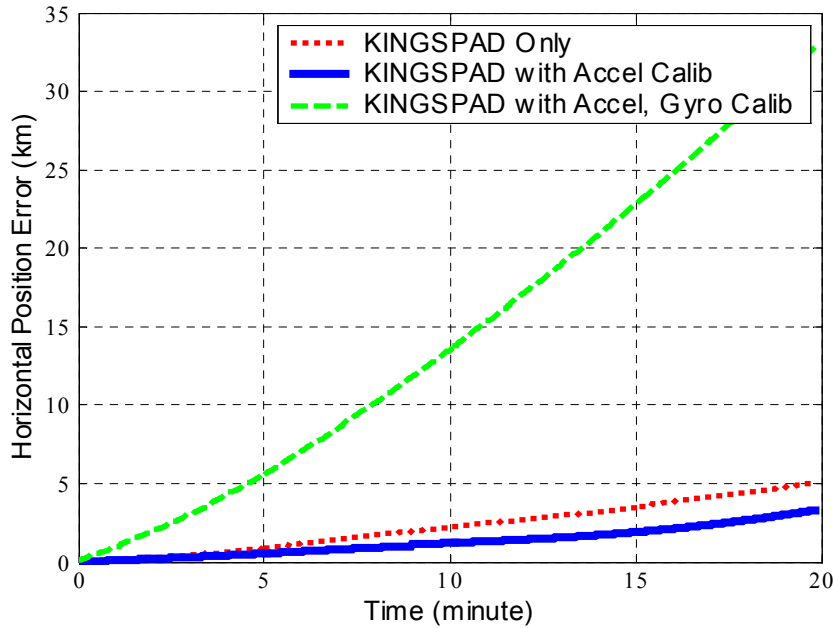
Figure 5.6: Effect of calibration on positioning (Test #1)

each of which were measured for two minutes works very well. However, when the gyroscope

calibration results were used together with the accelerometer calibration results, the error

increases rapidly and reaches 35 km in 20 minutes which corresponds to the error in one

hour for a tactical-grade IMU. One reason for this large positioning error is the short time of

each attitude measurement of the calibration and this leads to over-estimating the gyroscope

biases, which in turn resulted in wrong heading initialization and accumulation of the heading

error. On the other hand, the fifteen-state Kalman filter of the KINGSPAD™ software

tries to estimate the accelerometer and gyroscope biases during the fine alignment period.

However, it could not estimate the biases successfully, which is expected because the biases

are weakly observable components. Therefore, the bias estimation power of the fifteen-state Kalman is very weak and the estimation of the biases should be done separately.

For the second dataset, the measurement time for each calibration attitude has been increased to three minutes. Figures 5.7 and 5.8 show the same test results for the second dataset. Without using any calibration information, the horizontal positioning error reached about
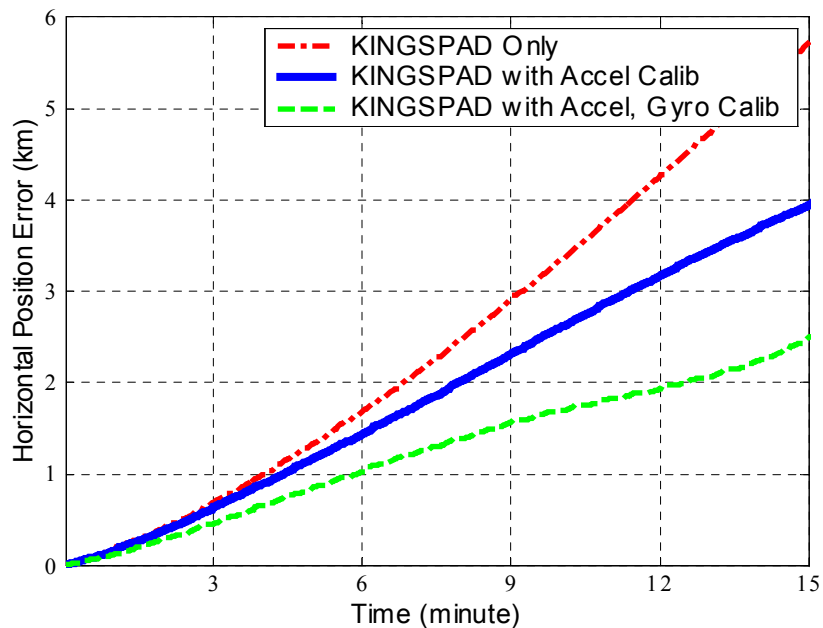

Figure 5.7: Effect of calibration on positioning (Test #2, 15 minutes)

5.8 km in 15 minutes, see Figure 5.7. The accelerometer calibration reduced the positioning error to 4 km (about 1.8 km reduction) in 15 minutes and together with the gyroscope calibration information the improvement in position is about 3.3 km in 15 minutes. Hence, when the calibration measurement time was increased to about 3 minutes, gyroscope noise

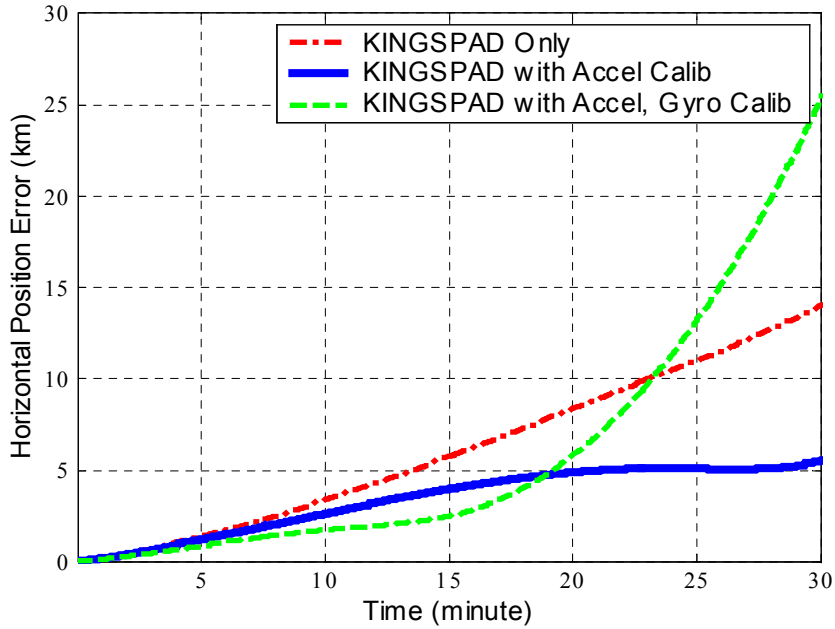could be removed significantly, which resulted in better estimation of biases.

Figure 5.8: Effect of calibration on positioning (Test #2)

However, as shown in Figure 5.8, after 18 minutes free inertial navigation the positioning error starts to grow rapidly, if the accelerometer and gyroscope calibration results were used together. This indicates that there are small amount of over-estimated gyroscope biases still remaining, and this causes accumulation of the heading error, which results in unbounded positioning error, in the integration process of the INS mechanization. This can be clearly identified from the fact that the standard deviation of the estimated z-gyroscope bias is about 0.17 deg/hr, which is larger by 0.1 deg/hr than those of the other channels, see Table 5.4. Therefore, for a long free inertial operation, longer measurement time for each attitude

is needed, at least 5 minutes. The figure also shows that when the accelerometer calibration results only were used, the error was about 6 km in 30 minutes. However, when no calibration information was applied, the error reached about 14 km in 30 minutes. Hence, accelerometer calibration removed over half of the positioning error.

5.5   INS Mechanization Performance

To check the performance of the INS mechanization developed in this thesis, the results of the mechanization in free inertial navigation mode, was compared with those of the KINGSPAD $^{\text{TM}}$ software. In this comparison, both mechanizations use the same initial position and attitude information, with only applying the bias compensation using the calibration results given in Table 5.4. The only difference between the two INS mechanizations, except for the calculation frame, is that the navigation frame mechanization considers the variation in sampling rate discussed in Section 2.3. Figures 5.9 and 5.10 show the horizontal position error of both INS mechanizations for the first and second test, respectively.

Recall that the first test was conducted with almost constant velocity about 30 km/hr, while the second test with higher acceleration and velocity range 20∼70 km/hr. In the first test, see Figure 5.9, the navigation frame mechanization shows better results (1.6 km horizontal positioning error in 20 minutes) than the KINGSPAD$^{\text{TM}}$ software (3.4 km horizontal posi-
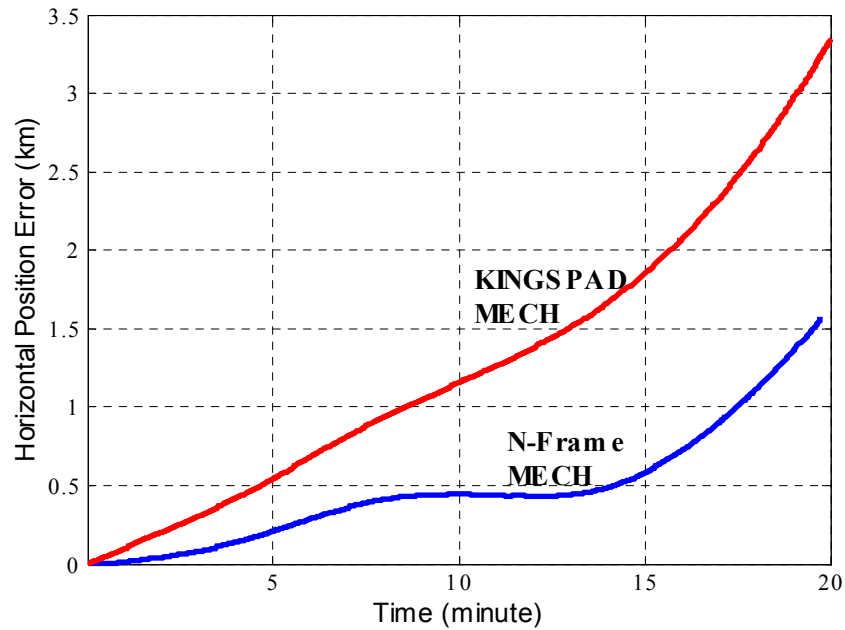
Figure 5.9: Mechanization performance (Test #1)

tioning error in 20 minutes). In the second test, see Figure 5.10, both mechanizations show similar performance. If both tests were extended to one hour, the positioning error for both mechanizations would reach about $30 \sim 40\ km$, which is almost the expected performance of the tactical-grade IMUs.
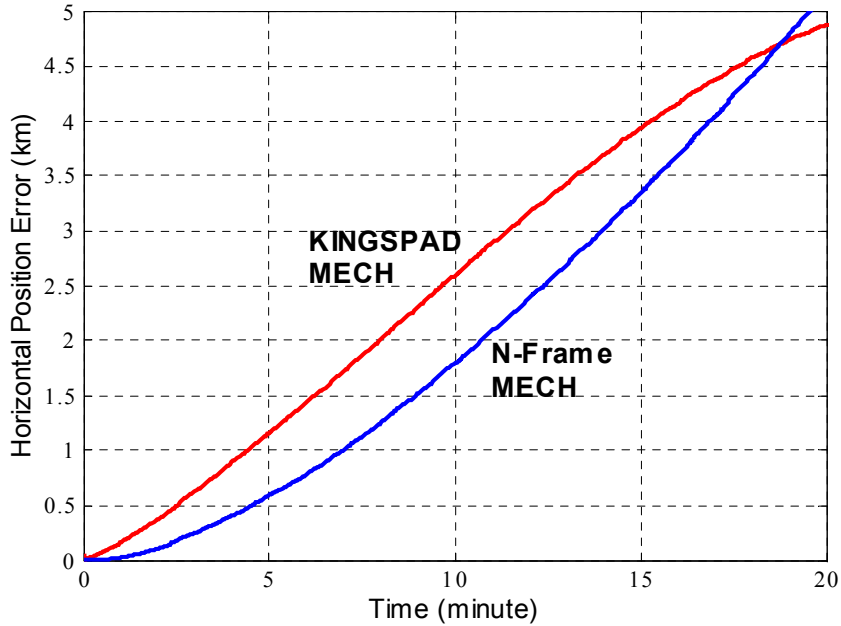
Figure 5.10: Mechanization performance (Test #2)

5.6   Velocity Matching Alignment

As mentioned in Section 4.2.3, the velocity matching alignment uses external velocity information to align the IMU while in motion, in this case GPS derived velocities. The GPS velocity measurement noise and PDOP during the velocity matching alignment calculation, obtained from the GrafNav software, are shown in Figures 5.11 and 5.12, respectively.

The standard deviation of the velocity looks high, because 0.25 m/s Doppler measurement standard deviation was used to prevent the position from being corrupted by erroneous Doppler measurements. Although Doppler measurements can be much more accurate, even
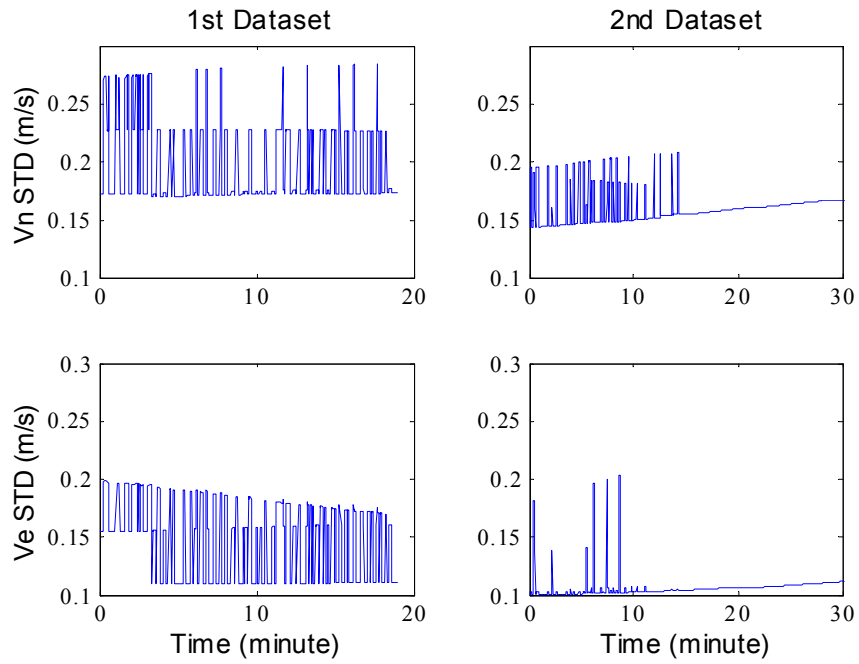
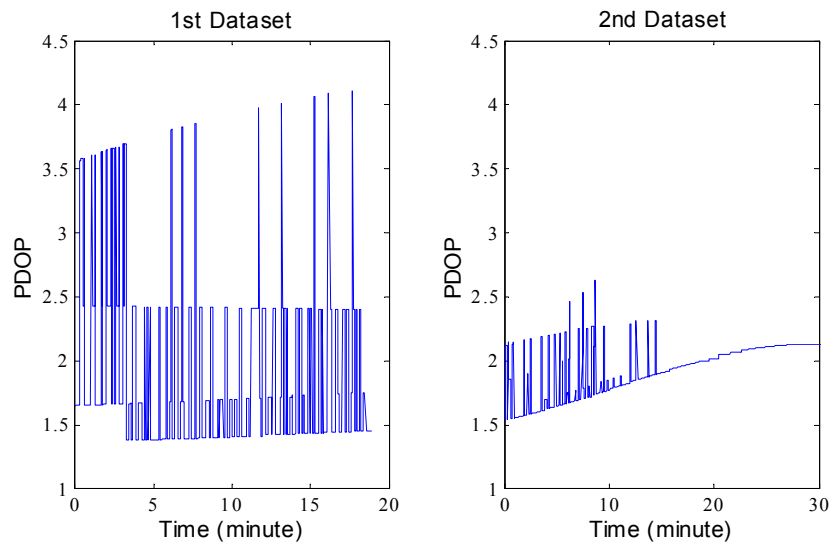Figure 5.11: GPS velocity measurement noise

Figure 5.12: PDOP during the velocity matching alignment

during the best of times there can be spikes as satellites rise or there are cycle slips (Cosandier, D. 2001, private communication). The variations in the velocity standard deviation look similar to those of the PDOP. Therefore, the GPS velocity solution depends on the geometry of the satellites.

Figure 5.13 and Table 5.5 show the attitude corrections applied to the navigator during the velocity matching alignment for both datasets. It can be clearly identified that all the attitude components converged within three minutes and the level of RMS after convergence is about 0.03°.

Table 5.5: Attitude corrections after 5 minutes

	1st dataset			2nd dataset		
	Roll	Pitch	Heading	Roll	Pitch	Heading
Mean (°)	0.0006	-0.0073	0.0003	0.0140	-0.0173	0.0003
STD (°)	0.0262	0.0089	0.0292	0.0347	0.0271	0.0354
RMS (°)	0.0262	0.0115	0.0292	0.0374	0.0321	0.0355

Figure 5.14 and Table 5.6 show the residuals during the velocity matching alignment for both datasets. The level of RMS is under 1 m/s and the maximum is within ±2 m/s (7.2 km/hr). This indicates the minimum velocity of the host vehicle for the velocity matching alignment. Therefore, the host vehicle can be driven slowly in an open area for three minutes
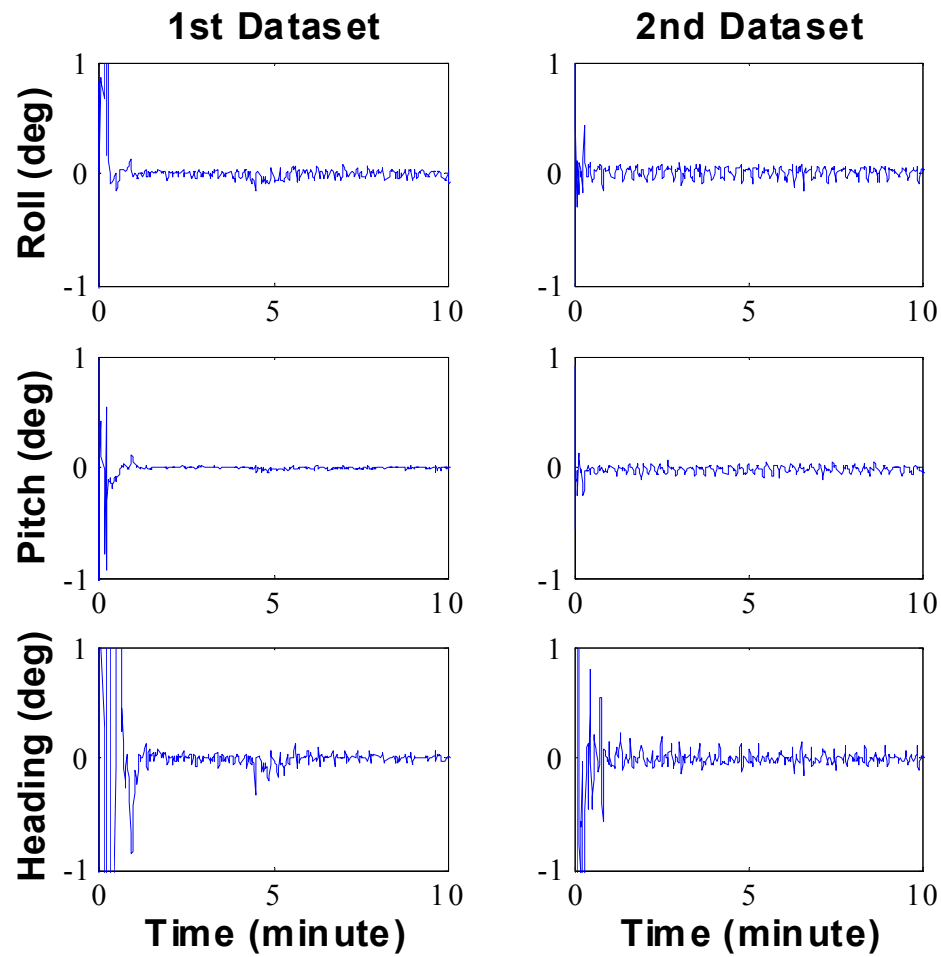
Figure 5.13: Attitude corrections

to align low cost IMUs. However, for lower grade IMUs, the minimum speed will be larger, because the residual will increase due the low quality of the sensors.
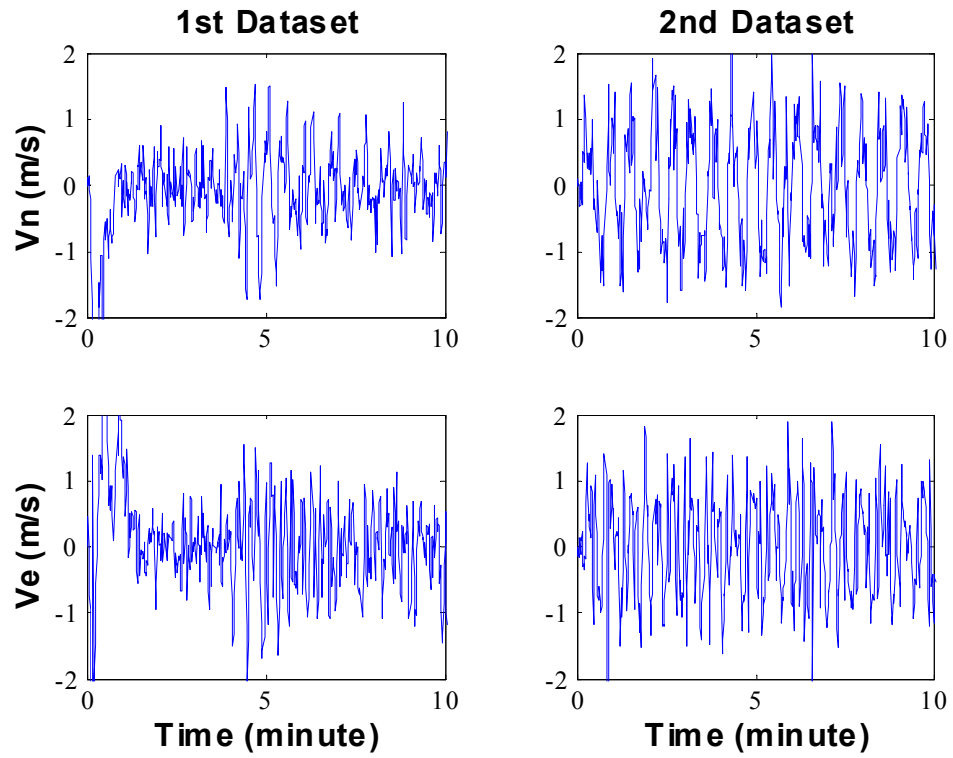
Figure 5.14: Velocity matching alignment residuals

Table 5.6: Velocity matching alignment residuals after 5 minutes

	1st dataset		2nd dataset	
	v_n	v_e	v_n	v_e
Mean (m/s)	-0.0112	-0.0119	-0.0348	0.0022
STD (m/s)	0.4920	0.5293	0.8409	0.6612
RMS (m/s)	0.4921	0.5294	0.8416	0.6612

5.7   Test of Non-Holonomic Constraints

Non-holonomic constraints were tested with the accelerometer calibration results only. Since lateral and up/down direction velocities cannot be zero in all operational conditions, the velocity measurement noise should be defined for realistic results. As shown in Figure 5.15, the misalignment of the IMU with respect to the vehicle forward direction causes $v \sin \theta$ velocity measurements for the lateral and up/down axes, where v is the vehicle velocity and θ is the misalignment angle. For a vehicle moving with a velocity of 60 km/hr and a misalignment angle of 10°, the lateral and up/down velocity measurements will be about 2.9 m/s. Therefore, velocity measurement noise of 1, 5, and 10 m/s will be used for the non-holonomic constraints in the Kalman filter.
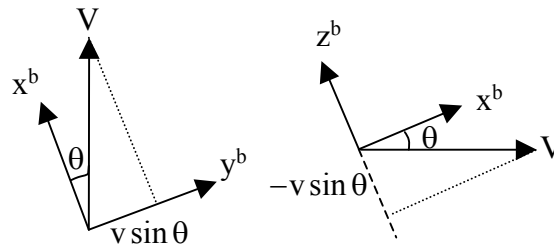

Figure 5.15: Misalignment of IMU to the vehicle forward direction

Figure 5.16 shows the horizontal positioning error for the first dataset when non-holonomic constraints were used as measurements in the Kalman filter. Similar to all other figures in the thesis, the reference trajectories were computed using the double-differenced GPS mea-
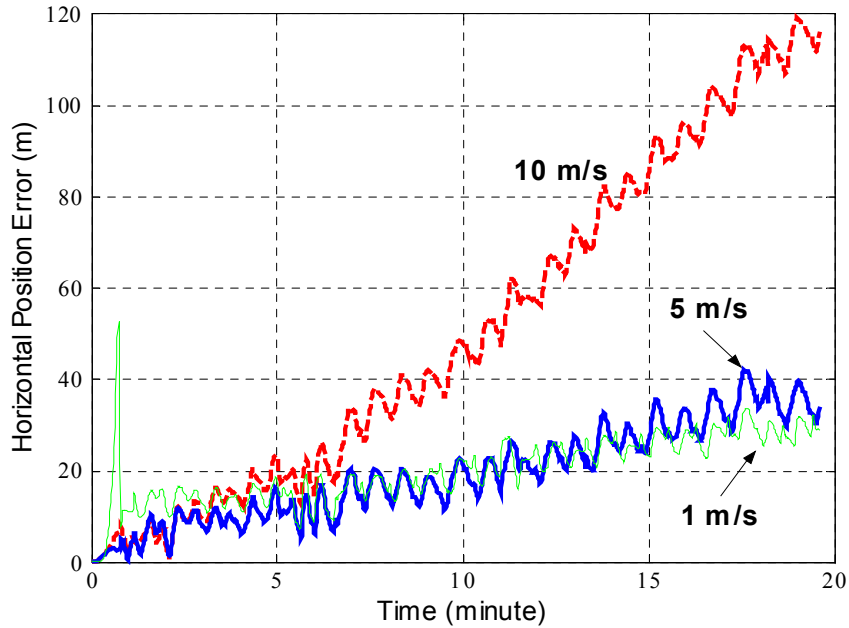
Figure 5.16: Test of nonholonomic constraints for the first dataset

surements. Two types of errors can be identified for all three conditions, i.e. the long-term linear trend and the short-term sinusoidal parts. The long-term linear parts are mainly from the vehicle's forward direction movement error due to the fact that the forward direction's velocity is not controlled by the non-holonomic constraints. The short-term sinusoidal errors are mainly due to the misalignment between the IMU and the vehicle's forward direction. But, the latter errors can also be generated due to the turning motion if the IMU is not installed at the vehicle's rotational centre. As shown in the figure, the horizontal positioning error reaches $120\ m$, $40\ m$, and $30\ m$ after 20 minutes for the $10\ m/s$, $5\ m/s$, and $1\ m/s$ velocity measurement noise, respectively. However, a large error spike ($50\ m$) can be identified

at the beginning of the first dataset when 1 m/s velocity noise was used. This could be due to the fact that, if the velocity measurement noise gets too small, the navigation Kalman filter considers real movement of the vehicle as errors.

Similar error patterns can be observed for the second dataset, see Figure 5.17. The horizontal
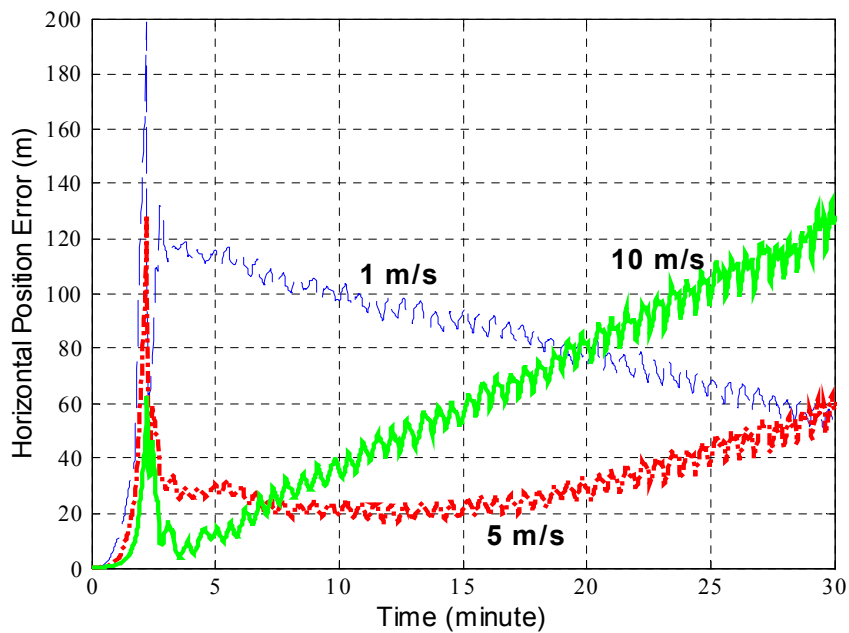

Figure 5.17: Test of nonholonomic constraints for the second dataset

positioning error reaches 130 m, 60 m, and 60 m after 30 minutes for the 10 m/s, 5 m/s, 1 m/s velocity measurement noise, respectively. However, an error spike is identified for all cases at the beginning of the test. The magnitude of this spike decreases as the velocity measurement noise increases. This is possibly due the specific manouevre of the vehicle at the beginning of the test. As shown in Figure 5.5, the vehicle was driven along the diagonal

direction of the parking lot to get higher acceleration. If the vehicle was driven faster in one direction (from upper-right to lower-left) and slower in the other direction (from lower-left to upper-right), then the positioning error from the over-constraining can be accumulated in one way. Furthermore, when 1 m/s velocity measurement noise was used, the positioning error decreased after the spike, which is quite unrealistic. Hence, 5 m/s measurement noise looks reasonable for this dataset. The results obtained from applying the non-holonomic constraints indicate that low cost inertial systems with similar performance as the Honeywell HG1700 can be used as a stand-alone positioning system during long GPS outages of up to 10 minutes while maintaining positional accuracy of about 10-20 m, which is similar to GPS single point positioning accuracy.

Chapter 6

Conclusions and Recommendations

6.1 Summary

The major objectives of this research was to develop and test various methods to improve the navigation accuracy of low cost INS/GPS systems. The research led to the following major contributions:

- The development of a new calibration method, which can be used to calibrate strapdown IMUs either in the lab or in the field right before starting a mission

- The development of a navigation frame INS mechanization and the INS/GPS integration Kalman filter; A nine-state Kalman filter was used by removing biases from the

state vector, as they can be estimated by the new calibration method.

- The development of the velocity matching alignment technique and the use of non-holonomic constraints as measurements in the Kalman filter.

The following are the conclusions and recommendation drawn from the developments and tests conducted in this thesis.

6.2 Conclusions

1. The new calibration method:

   (a) A rotation scheme, which can be attainable using a two-degree-of-freedom rotational frame, was provided for the eighteen different attitude measurements. In the case that the IMU was strapped down without using a rotational frame, the accelerometer bias can be determined with tilt measurements, but the vertical channel accelerometer bias and all scale factors are not so reliably estimated. The gyroscope bias can be calibrated with only horizontal measurements in mid-latitude areas.

   (b) Although the method can include the non-orthogonality of the IMU axes as parameters, it is disregarded in the field calibration, because more varied attitude

measurements with longer time are needed and therefore it will take long time to calibrate a system.

(c) It is shown that the accelerometer bias can be dealt with deterministically using the new field calibration method even when the reference gravity value is not exactly known, since all the errors are transferred to the scale factors. Furthermore the new calibration method works the same way as the simple up/down measurement method in the determination of bias and scale factors.

(d) The accelerometer calibration can be done in the field with six or more different attitude measurements each of which takes about 2~3 minutes. However, the measurement time of each attitude for gyroscope calibration should be increased to 5 minutes. The accelerometer calibration reduces almost half of the positioning error. The gyroscope bias calibration can minimize the initial heading determination error.

2. The INS mechanization and navigation Kalman filter:

(a) A navigation frame INS mechanization was developed, which provides similar accuracy to that of the KINGSPAD$^{\text{TM}}$ software .

(b) Many issues, which have to be considered in the implementation of the INS/GPS Kalman filter, were discussed in details including the lever-arm effect, resolving time difference between the IMU and GPS measurements, and the feedback of

the estimated errors.

(c) Based on these developments, the velocity matching alignment technique and the non-holonomic constraints have been developed and tested.

3. Velocity matching alignment:

(a) If the expected gyroscope biases are larger than 2 deg/hr, for example low-end tactical IMUs, and the field calibration is failed or not done, the velocity matching alignment would provide better attitude information than the stationary alignment technique.

(b) The tests of the velocity matching alignment technique show that all the attitude components converge within three minutes with an RMS of 0.03°.

4. The use of non-holonomic constraints:

(a) The measurement equations for non-holonomic constraints were developed strictly based on the perturbation analysis.

(b) The stand-alone INS positioning accuracy can be dramatically improved without augmenting any other sensors.

(c) Low cost IMUs can be used as a stand-alone positioning tool during GPS outages of over 10 minutes using the non-holonomic constraints. Within this time, the attainable accuracy is similar to what GPS single point positioning can provide ($10 \sim 20$ m).

(d) To minimize the error in applying the non-holonomic constraint, the IMU should be installed as close as possible to the vehicle's rotational centre and it should be closely aligned to the forward direction.

6.3 Recommendations

1. For those IMUs whose biases vary with temperature changes such as the Crossbow DMU-FOG IMU, it is recommended to use the new calibration method frequently during the survey mission to trace the change of biases.

2. Among various sensors to be augmented to the INS/GPS systems, odometers and speedometers are promising. Since almost all ground vehicles are equipped with these sensors already, it can be augmented without spending much extra efforts or expenses. In addition, these sensors can reduce significant amount of the forward motion errors still remaining after applying the non-holonomic constraints. These sensors can also be used to trigger the zero velocity updates.

3. Together with the odometers or speedometers, digital maps can aid low cost IMUs during long GPS outages, and therefore, without using any heading sensor, dead reckoning navigation is possible.

4. For the calibration of gyroscopes, other approaches, such as the Kalman filter formula-

tion of the new calibration method, can be investigated to reduce the estimation time in noisy environment.

5. For automotive-grade or consumer-grade IMUs, the method to limit the attitude error growth when the vehicle is not moving, was proposed in Section 4.4. However, it could not be tested due to the lack of instruments, especially the time tagging board. This method is highly recommended for future research and further testing.

References

Britting, K. R. (1971). *Inertial Navigation Systems Analysis.* John Wiley & Sons, Inc.

Brown, R. G. and Hwang, P. Y. C. (1992). *Introduction to Random Signals and Applied Kalman Filtering.* John Wiley & Sons, Inc., second edition.

Chatfield, A. B. (1997). *Fundamentals of High Accuracy Inertial Navigation.* American Institude of Aeronautics and Astronautics, Inc.

Conte, S. D. and de Boor, C. (1980). *Elementary Numerical Analysis: An Algorithmic Approach.* McGraw–Hill, third edition.

Farrell, J. A. and Barth, M. (1998). *The Global Positioning System & Inertial Navigation.* McGraw–Hill.

Gebre-Egziabher, D., Powell, J. D., and Enge, P. K. (2001). Design and performance analysis of a low–cost aided dead reckoning navigation system. In *In-*

ternational Conference on Integrated Navigation Systems, St. Petersburg, Russia. http://waas.stanford.edu/~www/gebre/papers/drsystem/ drsystem.pdf.

Gelb, A., Kasper Jr., J. F., Nash Jr., R. A., Price, C. F., and Sutherland Jr., A. A. (1974). *Applied Optimal Estimation*. The M. I. T. Press.

Greenspan, R. L. (1995). Inertial navigation technology from 1970–1995. *Navigation: Journal of The Institute of navigation*, **42**(1), 165–185. Special Issue.

Grewal, M. S., Weill, L. R., and Andrews, A. P. (2001). *Global Positioning Systems, Inertial Navigation, and Integration*. John Wiley & Sons, Inc.

Krakiwsky, E. J. (1990). *The Method of Least Squares: A Synthesis of Advances*. Dept. of Geomatics Eng., The University of Calgary, Calgary, Canada.

Litmanovich, Y. A., Lesyuchevsky, V. M., and Gusinsky, V. Z. (2000). Two new classes of strapdown navigation algorithms. *Journal of Guidance, Control, and Dynamics*, **23**(1), 34–44.

Maybeck, P. S. (1994). *Stochastic Models, Estimation, and Control: Volume 1*. Navtech Book & Software Store.

Mohamed, A. H. (1999). *Optimizing the Estimation Procedure in INS/GPS Integration for Kinematic Applications*. UCGE Reports Number 20127, Dept. of Geomatics Engineering, The University of Calgary, Calgary, Canada.

NovAtel, Inc. (2001). *Black Diamond System (BDS^{TM}) User Manual*, revision 0C edition.

Rogers, R. M. (2000). *Applied Mathematics in Integrated Navigation Systems*. American Institute of Aeronautics and Astonautics, Inc.

Salychev, O. S. (1998). *Inertial Systems in Navigation and Geophysics*. Bauman MSTU Press, Moscow.

Salychev, O. S., Voronov, V. V., Cannon, M. E., Nayak, N., and Lachapelle, G. (2000). Low cost INS/GPS integration: Concepts and testing. In *Proceedings of the ION National Technical Meeting*, pages 98–105, Anaheim, CA.

Savage, P. G. (1998a). Strapdown inertial navigation integration algorithm design part 1: Attitude algorithms. *Journal of Guidance, Control, and Dynamics*, **21**(1), 19–28.

Savage, P. G. (1998b). Strapdown inertial navigation integration algorithm design part 2: Velocity and position. *Journal of Guidance, Control, and Dynamics*, **21**(2), 208–221.

Schwarz, K.-P. (1999). *Fundamentals of Geodesy: Lecture Notes ENGO 421*. Dept. of Geomatics Eng., The University of Calgary, Calgary, Canada.

Schwarz, K.-P. and El-Sheimy, N. (1999). *Future Positioning and Navigation Technologies*. Dept. of Geomatics Eng., The University of Calgary, Calgary, Canada.

Schwarz, K.-P. and El-Sheimy, N. (2000). *KINGSPAD^{TM} Users Manual*. Dept. of Geomatics Eng., The University of Calgary, Canada, Version 3.0 edition.

Schwarz, K.-P. and Wei, M. (2000). *INS/GPS Integration for Geodetic Applications: Lecture Notes ENGO 623*. Dept. of Geomatics Eng., The University of Calgary, Calgary, Canada.

Shin, E.-H. and El-Sheimy, N. (2002). A new calibration method for strapdown inertial navigation systems. *Zeitschrift für Vermessungswesen*, **127**(1), 1–10.

Škaloud, J., Li, Y. C., and Schwarz, K.-P. (1997). Airborne testing of a C-MIGITS II – low cost integrated GPS/INS. In *Proceedings on International Symposium on Kinematic Systems in Geodesy, Geomatics and Navigation*, pages 161–166, Banff, Canada.

Sukkarieh, S. (2000). *Low Cost, High Integrity, Aided Inertial Navigation Systems for Autonomous Land Vehicles*. Ph.D. Thesis, Australian Centre for Field Robotics, Dept. of Mechanical and Mechatronic Engineering, The University of Sydney, Sydney, Australia.

Titterton, D. H. and Weston, J. L. (1997). *Strapdown Inertial Navigation Technology*. Peter Peregrinus Ltd.

Waypoint Consulting, Inc. (2000). *GrafNav/GrafNet, GrafNav Lite, GrafMov, GrafAtt Operating Manual*. 200 Rivercrest Drive S.E., Calgary, Alberta, Canada, Version 6.02 edition.

Wolf, R., Eissfeller, B., and Hein, G. W. (1997). A Kalman filter for the integration of a low cost INS and an attitude GPS. In *Proceedings on International Symposium on Kinematic Systems in Geodesy, Geomatics and Navigation*, pages 143–150, Banff, Canada.

Zhang, G. (1995). *A Low Cost Integrated INS/GPS System.* UCGE Reports Number 20078, The University of Calgary, Calgary, Alberta, Canada.